ACSNANO

www.acsnano.org

ARTICLE

Bioresorbable, Miniaturized Porous Silicon Needles on a Flexible Water-Soluble Backing for Unobtrusive, Sustained Delivery of Chemotherapy

Hyungjun Kim,[#] Heung Soo Lee,[#] Yale Jeon, Woohyun Park, Yue Zhang, Bongjoong Kim, Hanmin Jang, Baoxing Xu, Yoon Yeo,[*] Dong Rip Kim,[*] and Chi Hwan Lee[*]

Cite This: https://dx.doi.org/10.1021/acsnano.0c02343

Read Online

ACCESS | Metrics & More | Article Recommendations | Supporting Information

ABSTRACT: **Conventional melanoma therapies suffer from the toxicity and side effects of repeated treatments due to the aggressive and recurrent nature of melanoma cells. Less-invasive topical chemotherapies by utilizing polymeric microneedles have emerged as an alternative, but the sustained, long-lasting release of drug cargos remains challenging. In addition, the size of the microneedles is relatively bulky for the small, curvilinear, and exceptionally sensitive cornea for the treatment of ocular melanoma. Here, we report a design of bioresorbable, miniaturized porous-silicon (p-Si) needles with covalently linked drug cargos at doses comparable to those of conventional polymeric microneedles. The p-Si needles are built on a water-soluble film as a temporary flexible holder that can be intimately interfaced with the irregular surface of living tissues, followed by complete dissolution with saline solution within 1 min. Consequently, the p-Si needles remain embedded inside tissues and then undergo gradual degradation, allowing for sustained release of the drug cargos. Its utility in unobtrusive topical delivery of chemotherapy with minimal side effects is demonstrated in a murine melanoma model.**

KEYWORDS: *melanoma treatment, topical drug delivery, bioresorbable silicon nanomaterials, sustained drug release, minimally invasive injection*

Melanoma—the most serious form of skin cancer—is typically caused by ultraviolet radiation from natural sunshine or tanning beds and developed at the stratum corneum of epidermis (15−25 μm from the skin surface).[1] Given the aggressive and recurrent nature of melanoma cells, repeated treatments are often necessary, thereby increasing the risk of toxicity and side effects.[2] An effective treatment involves using the topical administration of chemotherapeutics into tumor tissues using polymeric microneedles as a less-invasive and painless route.[3,4] Recently, further miniaturized nanoscale needles made of porous-silicon (p-Si) emerge as an attractive candidate for intratissue injection that can offer a favorable safety profile and controlled biodegradability.[5−7] Compared to conventional polymeric microneedles, the miniaturized p-Si needles benefit from their amenability to existing nanofabrication processing and therefore provide the following key advantages: (1) precise control of the size, geometry, tapering, and tip morphology at the nanoscale,[8] (2) rational tuning of porosity on the surface (in turn, drug loading capacity),[6,9] (3) preprogrammable dissolution rate of the p-Si needles through surface oxidations (encapsulation),[10,11] (4) uniform delivery owing to the high density of the p-Si needles per projected surface area,[5] and (5) long-lasting release of covalently linked drug cargos by gradual degradation of the p-Si needles in tissue fluids over time.[9,12] These attributes are important for controlled, sustained, and minimally invasive topical delivery of therapeutics.

However, challenges still remain in that the vertically ordered arrays of the p-Si needles are built on a rigid Si wafer that can accommodate the conditions required for conventional nanofabrication processing such as thermal annealing, corrosive chemical etching, and photolithographic patterning.[13] The use of the rigid Si wafer results in a mechanical mismatch when interfaced with the soft, curvilinear, and dynamic surface of living tissues. This discordance

Received: March 18, 2020
Accepted: May 13, 2020
Published: May 13, 2020

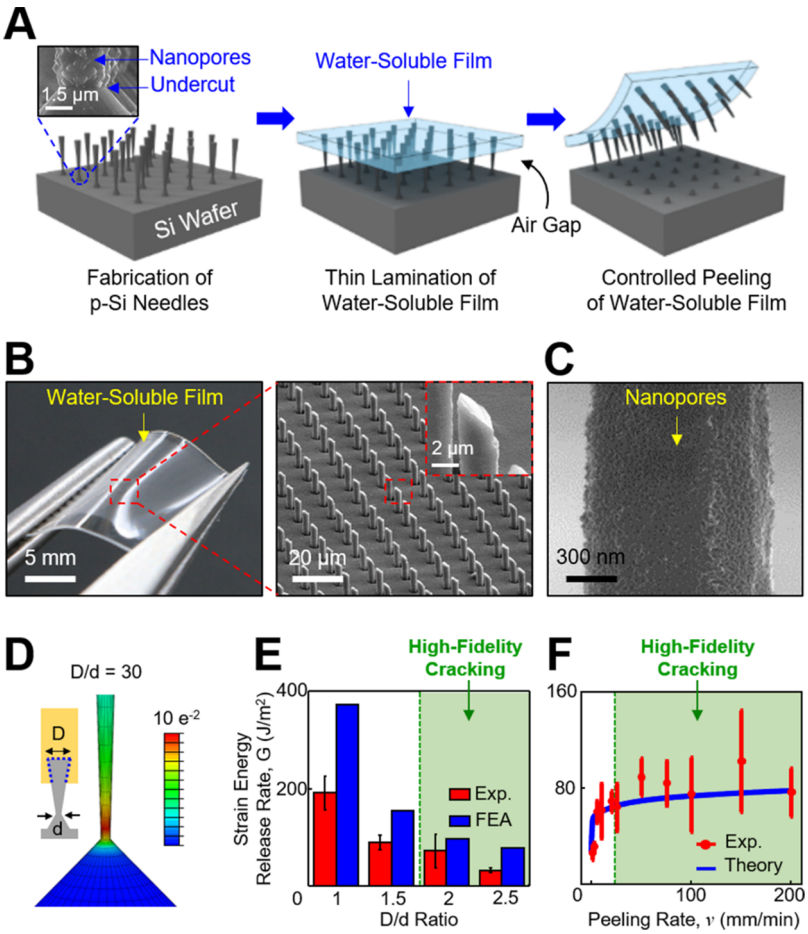

Figure 1. Design principle and fabrication process. (A) Schematic illustrations for the construction of the p-Si needles on a water-soluble backing. The inset image highlights the bottom undercut and nanopores at the bottom and on the surface of the p-Si needles, respectively. (B) Optical images of the p-Si needles integrated with a PVA film. The inset image highlights the sharpened angular tip of the p-Si needles. (C) SEM image of the nanopores formed on the surface of the p-Si needles. (D) Representative FEA results showing the distribution of principal strains along the p-Si needle during constant peeling. (E) Experimental and FEA results for the effect of D/d ratio on strain energy release rate (G). (F) Experimental and theoretical results for the effect of peeling rate (v) on G.

leads to debasing of the interfacial contact quality, which is particularly problematic in their application to the small, curvilinear, and exceptionally sensitive cornea, where melanoma is occasionally formed (*i.e.*, ocular melanomas).[14] Our recent work demonstrated that these challenges can be alleviated to some extent by building the miniaturized p-Si needles on a thin, flexible backing film made of silicone elastomer such as polydimethylsiloxane (PDMS) for their use in intracellular drug delivery.[15] A disadvantage of this construct is that the flexible PDMS backing film may cause irritation or discomfort to the wearer especially under vigorous deformations of tissues by body movements. Complete elimination of the backing film after the insertion of the p-Si needles into tissues may resolve the physical strain, thereby enabling unobtrusive topical delivery of therapeutics over a prolonged period of time.

Here, we introduce a bioresorbable, miniaturized p-Si needle loaded with covalently linked drug cargos, which is built on a thin, flexible, and water-soluble film. The water-soluble film is temporarily used during the insertion of the p-Si needles into tissues and then can be immediately dissolved within 1 min by the application of saline solution. Consequently, the p-Si needles remain embedded inside tissues and, due to the nanoscale size, become unobtrusive (nearly unnoticeable) to the wearers without affecting their natural motions. The p-Si needles subsequently undergo gradual hydrolysis in tissue fluids to degrade into biocompatible byproducts, leading to sustained, long-lasting release of preloaded drug cargos over days at a controlled rate. Comprehensive experimental and computational studies provide insight into the structural design and construction of the p-Si needles on a water-soluble backing over centimeter-scale areas and elucidate the fundamental attributes. Demonstrations of the p-Si needles for the topical delivery of chemotherapy in a murine melanoma model illustrate the utility of this concept.

RESULTS AND DISCUSSION

Design Principle and Fabrication Process. Figure 1A schematically illustrates the basic procedure to integrate the bioresorbable, miniaturized p-Si needles with a thin, flexible, and water-soluble medical film such as poly(vinyl alcohol) (PVA; medical-grade; mechanical modulus (E) = 3.4 GPa; molecular weight of ~31 000; Sigma-Aldrich, USA). The first step is to fabricate an array of vertically ordered p-Si needles on a polished monocrystalline Si wafer through sequential steps of photolithographic patterning, dry and wet etchings, and metal-assisted chemical etching (MACE) (Figure 1A, left).[15] This step also formed uniform undercuts and nanopores at the

https://dx.doi.org/10.1021/acsnano.0c02343
ACS Nano XXXX, XXX, XXX−XXX

bottom and on the surface of the p-Si needles, respectively (inset image). Details of the fabrication procedures are shown in the Materials and Methods section. Figure S1 shows representative scanning electron microscopy (SEM) images of the as-fabricated p-Si needles, exhibiting a minimum tip diameter (d) of 150 nm, a base diameter (D) of 2−4 μm, and a length (L) of 10−70 μm. In the next step, the entire structure was spin-cast with 10 wt % PVA (200−300 μm thick), allowing an air gap to form at the interface due to surface tension (Figure 1A, middle). The length of the p-Si needles was determined by this air gap that was adjusted by controlling the spin-casting speed within the range from 300 to 500 rpm, leading to the consequent air gap size of ∼20 μm and ∼50 μm, respectively (Figure S2). The spin-casting of the PVA film was repeated until its total thickness reached about 200−300 μm to provide sufficient mechanical strength for handling. Subsequently, a thermal annealing was followed to complete the solidification of the PVA film using a convection oven maintained at 70 °C for 30 min. Finally, the fully cured PVA film was peeled from the Si wafer at a constant peeling rate of 50 mm/min using an automated peeling apparatus (Mark-10, Willrich Precision Instrument) (Figure 1A, right). During this peeling process, mechanical stress can be concentrated predominantly at the bottom undercuts of the p-Si needles to generate cracks allowing for their physical liberation from the Si wafer.[15]

Figure 1B shows representative photograph (left) and enlarged microscope image (right) of the physically transferred p-Si needles to a thin layer (200−300 μm thick) of a PVA film. The intrinsically thin and flexible property of the PVA film can facilitate intimate contact to the soft, irregular surface of tissues, while the sharpened angular tip of the p-Si needles facilitates easier penetration.[15,16] The overall height, vertical arrangement, and tip morphology of the transferred p-Si needles were consistent across the entire specimen area (3 × 3 cm^2). Figure S3 shows the fractured planes on both the donor Si wafer and the receiver PVA film, suggesting that the cracking occurred uniformly at the bottom undercut of the p-Si needles. Figure 1C shows the nanopores formed on the surface of the p-Si needles in which the porosity (in turn, drug loading capacity) can be adjusted during the MACE process. The SEM images in Figure S4 provide representative examples of the p-Si needles configured into different surface porosities (0%, ∼30%, ∼45%, and ∼60%) that were controlled by the MACE time of 0, 30, 60, and 90 s, respectively. Figure S5 presents a series of optical images at various stages during the dissolution of the PVA film, colored with yellow food dye (McCormick & Company, USA) for visualization, when immersed in 50 mL of phosphate-buffered saline (PBS; pH 7.4; Sigma-Aldrich, USA) at 37.5 °C. The complete dissolution of the PVA film occurred typically within 10−15 min in this condition (Movie S1, Supporting Information), or it can be swabbed away using a saline-moistened cotton swab in less than 1 min.

The controlled cracking at the bottom undercut of the p-Si needles over centimeter-scale areas is crucial to successful implementation of this approach. Figure S6 shows an experimental setup and the corresponding experimental results for the peeling load−peeling distance curve for a specimen (1 × 1 cm^2, d = 1 μm, D = 4 μm, and L = 50 μm) under constant peeling of the PVA film at 50 mm/min. Movie S2 (Supporting Information) demonstrates the real-time measurement process. The results indicate that the peeling load increased rapidly to a maximum and initiates cracking and then reached a plateau for steady-state crack propagation. Figure 1D shows finite element analysis (FEA) results, revealing that the principal strain (ε) remained localized near the bottom undercut of the p-Si needles during the constant peeling. The tendency for the localization of ε was more evident as the D/d ratio was increased, wherein the peak principal strain (ε_{peak}) was larger than the fracture limit (∼1%) of the p-Si needles when D/d > 1.5 (Figure S7). The experimental and FEA results of strain energy release rate (G) for the cracking are summarized in Figure 1E. The green-filled area denotes where the cracking typically occurred with high fidelity. Figure 1F experimentally and theoretically reveals the dependence of G on peeling rate (v) of the PVA film. The results showed a clear power-law relationship of them (*i.e.*, the G increased rapidly at low v and then gradually reached steady state) due to the viscoelastic property of the PVA film.[17] For instance, a rapid peeling (v > 20 mm/min) of the PVA film provided sufficiently large adhesive strength to peel the p-Si needles away from the Si wafer. On the other hand, a slow peeling (v < 20 mm/min) of the PVA film was unable to hold the p-Si needles, resulting in compressed marks left on the surface (Figure S8). For the theoretical analysis, the energy release rate was obtained by assuming that the PVA film was monolithically bonded to the p-Si needles without embedding inside, causing the discrepancy with the experimental results especially at high peeling rate (v > 100 mm/min).

Controlled Dissolution of the p-Si Needles in Biological Fluids. Figure 2A show the gradual dissolution of a unit array (1 × 1 cm^2) of the p-Si needles with a fixed initial base diameter (D_0) of 3 μm when immersed in 50 mL of PBS (pH 7.4) at 37.5 °C for 90 days, while refreshing the solution every 10 days to maintain the pH value. The magnified SEM images of the p-Si needles at predetermined time interval are shown in Figure S9. The dissolution of the p-Si needles occurred *via* hydrolysis of Si to silicic acid and hydrogen (*i.e.*, $Si + 4H_2O \leftrightarrow Si(OH)_4 + 2H_2$), which involves nucleophilic attack at the surface to weaken the interior bonds of Si atoms.[18−20] The dissolution kinetics rely on the pH, temperature, and ionic strength of the solution as well as the predefined surface porosity of Si.[10] Figure 2B shows measurement results of the gradual diameter reduction (D/D_0) of the p-Si needles with varied surface porosities, indicating that the dissolution rate was increased from ∼10 nm/day to ∼20 nm/day as the surface porosity was increased from 0% to 60%. Figure 2C and D compare the dissolution of the p-Si needles in higher pH environment (PBS; pH 10.0) at 37.5 °C. The results indicate that the dissolution rate was substantially accelerated at higher pH, while the rate was nonlinearly decreased over time due to enhanced dependence on the concentration of the byproducts, such as $Si(OH)_4$, in the solution.[19] In fact, the biosafety of the monocrystalline Si nanomaterials and their dissolution products has been proved in many biomedical applications, without showing measurable cytotoxic effects.[10,11,19,20]

Figure 2E shows a series of snapshot images obtained from molecular dynamics (MD) simulation at different time frames, revealing the dissociation process of a Si atom (highlighted in blue) in water (H_2O) due to the effect of nucleophile attack by OH^- groups (enlarged). At the beginning (t = 0.5 ns), no bonding occurred between the Si atom and OH^- groups. At t = 3 ns, an OH^- group started attacking the Si atom to create a bond. At t = 4 ns, another OH^- group attacked the Si atom and formed another bond to break an interior Si−Si bond. At t

https://dx.doi.org/10.1021/acsnano.0c02343
ACS Nano XXXX, XXX, XXX−XXX

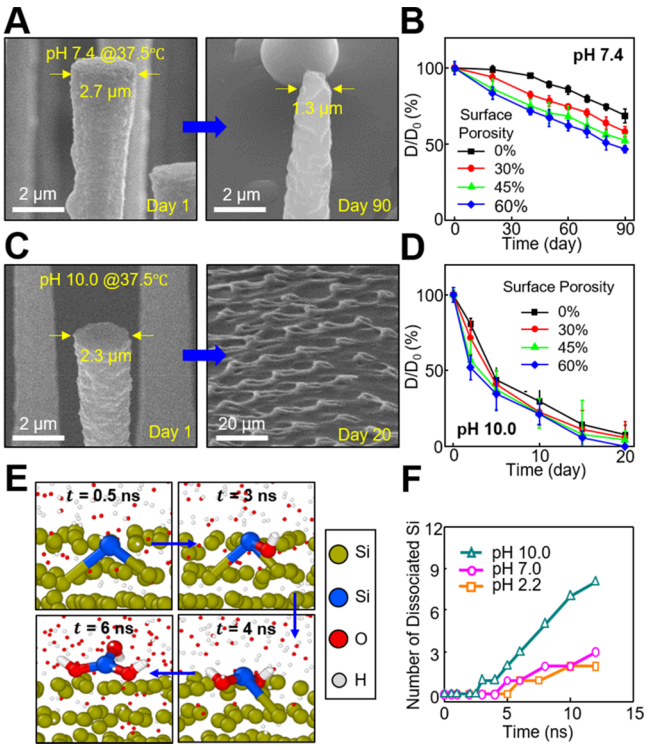

Figure 2. Degradation of the p-Si needles in biofluids. (A) SEM images of the p-Si needles at 1 day (left image) and 90 days (right image) after immersing in 50 mL of PBS (pH 7.4) at 37.5 °C. (B) Measurement results of D/D_0 ratio (%) obtained from the p-Si needles with varied surface porosities of 0% (black), 30% (red), 45% (green), and 60% (blue). (C) SEM images of the p-Si needles at 1 day (left image) and 20 days (right image) after immersing in 50 mL of PBS (pH 10.0) at 37.5 °C. (D) Measurement results of D/D_0 ratio (%) obtained from the p-Si needles with varied surface porosities. (E) Snapshot images of MD simulation at different time frames. (F) Results of the number of dissociated Si atoms in solutions at acidic (pH 2.2) and basic (pH 10.0) conditions formed by the addition of H^+ and OH^- groups, respectively, compared to a neutral condition (pH 7.0).

= 6 ns, one more OH^- group attacked the Si atom and finally triggered its complete dissociation. The dissociation occurred when the maximum distance of a Si atom from its nearest neighbors remained longer than 3.0 Å.[19] Figure 2F shows the variation of number of dissociated Si atoms in solutions at acidic (pH 2.2) and basic (pH 10.0) conditions formed by addition of H^+ and OH^- groups, respectively, compared to a neutral condition (pH 7.0). The results show that the number was increased over the simulation time from 0 to 12 ns, while the dissolution was accelerated at higher pH due to the increased concentration of OH^- groups. It is also anticipated that the enhanced surface porosity would also affect the reaction (dissolution) rate due to the increased contact area between the Si and liquid solution. These findings are consistent with the above-described experimental observations.

Biocompatibility and Controlled Drug Release. To evaluate *in vivo* tissue compatibility, a set of real-time bioluminescence images were captured at 5 h postinjection of the p-Si needles (1 × 1 cm^2, d = 150 nm, D = 1 μm, and L = 50 μm) to the epidermis (on top of the skin; top row) and subcutaneous muscle (under the skin; bottom row) on the backside of mice (Figure 3A). To compare the biocompatibility grade, the experiments were conducted using the p-Si needles built on a medical-grade PVA film (left column; Sigma-Aldrich, USA), ones on an industrial-grade PVA film (middle column; Fiber Glast, USA), and a positive control treatment (right column) of phorbol 12-myristate 13-acetate (PMA; 1 mM, 20 μL; Sigma-Aldrich, USA) that promotes intense local inflammation.[21] Both the epidermis and the subcutaneous muscle showed no evidence of inflammation following the administration of luminol (5-amino-2,3-dihydro-1,4-phthalazinedione), which detects acute inflammation at the implemented sites,[22] whereas acute inflammation appeared in the control mice. Here, the industrial-grade PVA was dissolved within 1 min after the insertion of the p-Si needles into the tissues by applying saline immediately, thereby causing no inflammation. Figure 3B shows *in vitro* cell viability of human dermal fibroblast (HDF) cells seeded in a 24-well plate (Fisher Scientific, USA) that contains the p-Si needles (1 × 1 cm^2, d = 150 nm, D = 2 μm, and L = 20 μm) and medical-grade PVA film (red bar), as measured using a colorimetric MTT assay kit (3-(4,5-dimethylthiazol-2-yl)-2,5-diphenyltetrazolium bromide, Sigma-Aldrich, USA). For these tests, the length of the p-Si needles (20 μm long) was tailored for the HDF cells, of which the average diameter is about 20−30 μm. The cell viability remained over 99.3% during the entire period (3 days) of the assay without substantial difference compared to that of the control bare medical-grade PVA film without the p-Si needles (blue bars), whereas acute toxicity appeared in the industrial-grade PVA film (green bars) due to the residual ethanol and butanol. Similar results were observed in other control specimens formed by replacing the PVA film with a sheet of water-soluble poly(lactic-*co*-glycolic acid) (PLGA; 50/50 lactide:glycolide; molecular weight = 30 000−60 000; E = 2 GPa; Sigma-Aldrich, USA), providing the cell viability of >97.4% (Figure S10).

Covalent conjugation of drug cargos to the surface of the p-Si needles is critical to reliable drug loading and sustained releasing behavior.[9,12] Figure 3C shows representative fluorescence microscopy images (top view) of the p-Si needles where the surface was covalently linked with the chemotherapy drug doxorubicin (DOX) *via* 3-triethoxysilylpropyl succinic anhydride (TESPSA, Gelest Inc., USA) as a cross-linker. The confocal lens (40×) was focused at the bottom of the p-Si needles, resulting in ring-shaped fluorescence of the DOX. The peak fluorescence intensity of the DOX was observed on the surface of the p-Si needles due to the high surface area of the nanopores. Figure 3D shows a three-dimensional (3D) confocal image (tilted view) of the p-Si needles upon insertion into a soft agarose gel (2.8% w/v) that provides a comparable mechanical modulus (E ≈ 100 kPa) to the human tissues (E = 80−150 kPa). The experiments were performed by gently pressing the PVA film with the p-Si needles (1 × 1 cm^2, d = 150 nm, D = 1 μm, and L = 50 μm) into the agarose gel, followed by the application of saline to completely dissolve the PVA film. The side view of the image (bottom row) highlights that the p-Si needles were embedded inside the agarose gel through the full length of 50 μm. The larger-field views of the specimen are shown in Figure S11.

Figure 3E shows the total cumulative amount of DOX released from the p-Si needles with varied surface porosities of 0−60% in PBS (pH 7.4) at 37.5 °C. The corresponding release profiles as a function of time (up to 100 h) are shown in Figure 3F, exhibiting that rapid release of DOX occurred within 24 h and then gradually reached a plateau at the predefined doses. The range of the released doses (18−35 μg) was comparable

https://dx.doi.org/10.1021/acsnano.0c02343
ACS Nano XXXX, XXX, XXX−XXX

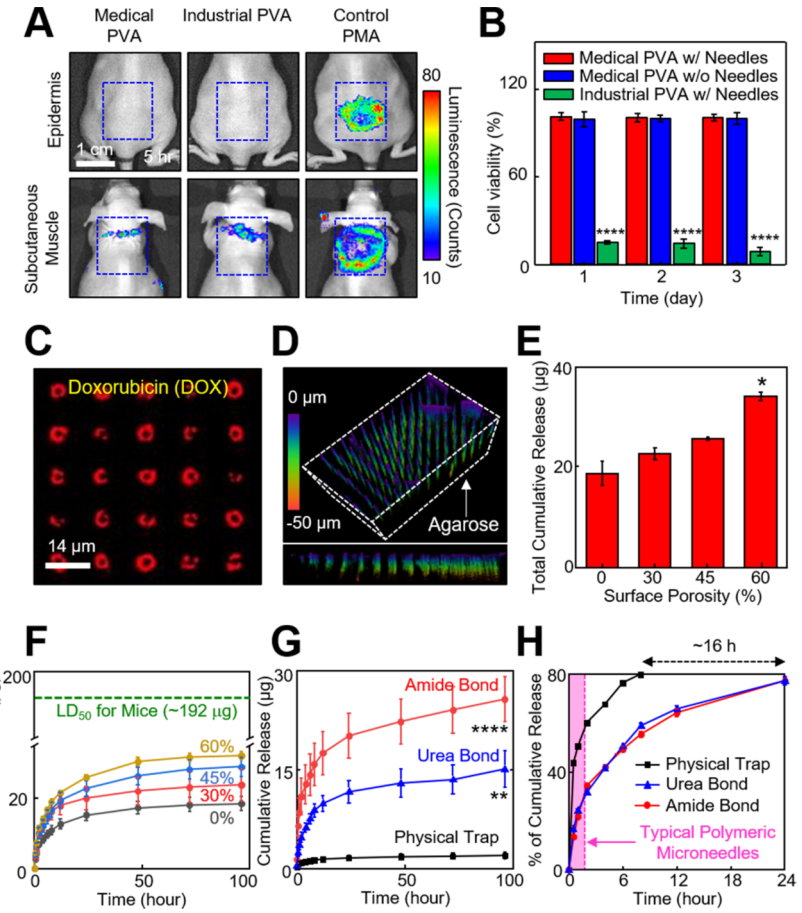

Figure 3. Biocompatibility and controlled drug release. (A) Real-time bioluminescence images on the epidermis (on top of the skin) and subcutaneous muscle (under the skin) of mice at 5 h following the implementation of the p-Si needles built on a medical-grade PVA (left column), industrial-grade PVA (middle column), and control PMA treatments (right column). (B) Results of the MTT assay in the cytotoxicity tests of HDF cells incubated with a medical-grade PVA with (red bars) and without (blue bars) the p-Si needles, as well as an industrial-grade PVA (green bars). Error bars represent the standard deviation (SD) of three replicates. ****$p < 0.0001$ compared to the medical-grade PVA with the p-Si needles using one-way analysis of variance (ANOVA). (C) Confocal microscopy image of the p-Si needles loaded with DOX. (D) Confocal microscopy image of the p-Si needles embedded inside a 2.8% (w/v) agarose gel (color index by penetration length). (E) Cumulative release of DOX obtained from the p-Si needles with varied surface porosities of 0%, 30%, 45%, and 60% after 20 days of the immersion in PBS (pH 7.4) at 37.5 °C. *$p < 0.05$ compared to 0% surface porosity using ANOVA. (F) Release profiles obtained from the p-Si needles with covalently linked DOX, compared to median lethal dose of DOX in mice (LD_{50}, green dotted line). (G) Release profiles obtained from the p-Si needles with the surface porosity of ~45% using amide (red line), urea (blue line), and control physical (black line) bonds of DOX. **$p < 0.01$ and ****$p < 0.0001$ compared to the control physical bond using ANOVA. (H) Cumulative release (%) of the covalently linked (amide and urea bonds) DOX, compared to the control physically trapped DOX.

to those used in similar studies using polymeric microneedles.[23,24] Importantly, the released doses remained higher than the half-maximal inhibitory concentration (IC_{50}) value (~0.3 μg/mL) for B16F10 murine melanoma cells and substantially lower than the lethal dose (LD_{50}) value (~192 μg; green dashed line) for mice. Figure 3G shows the cumulative release of covalently linked DOX using different cross-linkers of amide (red line) and urea (blue line) in PBS (pH 7.4), as compared to that of physically trapped DOX (black line). For these tests, the surface porosity of the p-Si needles was fixed at ~45%. The amide and urea bonds are well known to provide strong covalent linkages of the amine group ($-NH_2$) of DOX to the succinic anhydride of TESPSA and the isocyanate ($-N{=}C{=}O$) of 3-isocyanatepropyltriethoxysilane (ICPTS), respectively.[25] The control physical bond relies on relatively weak van der Waals force, resulting in rapid and burst release of drug molecules.[26] The schematic diagrams of these bonding mechanisms are shown in Figure S12. The highest drug loading capacity occurred in the amide bond (~25 μg) followed by the urea bond (~15 μg), both of which were substantially higher than that of the physical trapping (~2 μg). These observations support that the covalently linked DOX provides strong binding affinity for the surface of the p-Si needles to form a highly stable complex at physiological pH.[37] The strong covalent boding is critical to the sustained release of DOX by allowing the release to occur predominantly by the gradual dissolution of the p-Si needles. Figure 3H presents the corresponding release profiles (%) as a function of time (up to 24 h), highlighting the longer-lasting release of the covalently linked DOX than counterparts. For instance, more than 80% of the covalently linked DOX was released for ~24 h (red and blue lines), which was substantially longer than control specimens with the physically bonded DOX (~8 h; black line) and conventional polymeric microneedles (typically, 15 min to 2 h; pink-filled area),[27] respectively.

https://dx.doi.org/10.1021/acsnano.0c02343
ACS Nano XXXX, XXX, XXX−XXX

Unobtrusive Topical Application of p-Si Needles. To illuminate the utility of the p-Si needles in the envisioned scenarios of transepidermal, transmuscular, and transocular injections, a unit array of the p-Si needles (1 × 1 cm^2, d = 150 nm, D = 1 μm, and L = 50 μm) with covalently linked (amide) fluorescent dyes (DyLight 800, Pierce Thermo Scientific) was introduced to the epidermis, subcutaneous muscle, and cornea of athymic nude mice *in vivo*. Details of the experimental procedures are shown in the Materials and Methods section. Figure 4A shows representative optical images, pointing out

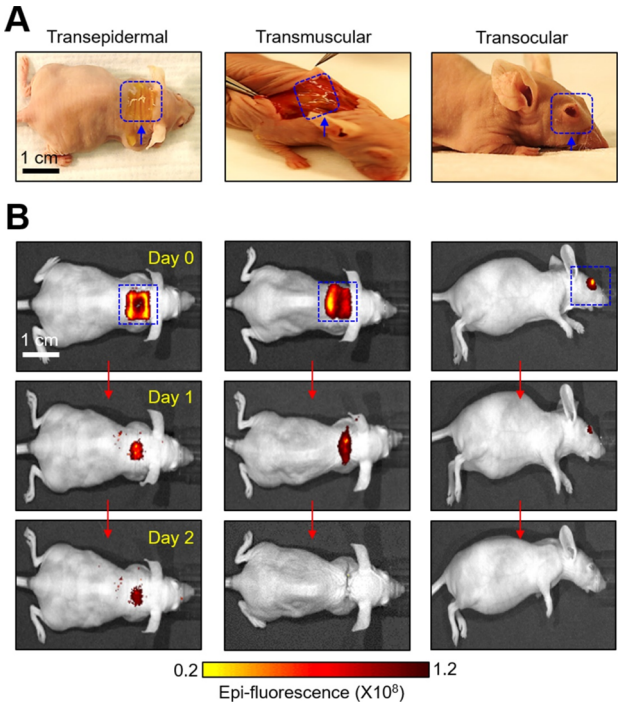

Figure 4. Unobtrusive topical delivery of the p-Si needles. (A) Optical images of the p-Si needles with DyLight 800 fluorescent dyes on a PVA film, applied to the epidermis (left image), subcutaneous muscle (middle image), and cornea (right image) of mice. (B) IVIS images of the mice receiving the p-Si needles for 2 days following the implementations.

the injection sites where the p-Si needles were embedded after the PVA film was completely dissolved with saline solution. The size of the p-Si needles was much smaller than that of conventionally used polymeric microneedles (typically, d > 5 μm, D > 300 μm, and L > 600 μm)[4,16,28,29] and remained nearly unnoticeable on the tissue surface by visual observations (Figure S13). This aspect may help reduce the risk of irritation or discomfort during/after the injection of the p-Si needles. The mice exhibited normal behaviors without showing any evidence of discomfort against natural movements for the entire period of observation (>3 months). Figure 4B shows the corresponding IVIS images, indicating that the fluorescent dyes were uniformly localized over the irregular surface of the epidermis, subcutaneous muscle, and cornea of the mice and maintained until the florescent dyes were completely absorbed into the body. Figure S14 shows optical images of a control unit array (1 × 1 cm^2) of the p-Si needles integrated with a flexible, yet non-water-soluble PDMS film (200 μm thick), which was attached on the back of a nude mouse. Of note, no wrinkles were observed on the skin over the PDMS film, while other areas of the skin were easily wrinkled according to body movements. These observations imply that the skin underneath the PDMS film experienced occasional interruptions or discomfort due to the physical constraints, highlighting the rationale of eliminating the backing film after complete delivery of the p-Si needles.

Demonstration on Postsurgical Melanoma Treatments in Mice *In Vivo*. Tumor relapse after surgical resection that often occurs by the outgrowth of residual microtumors remains a significant challenge in the treatment.[30] Systemic chemotherapy and radiotherapy are often employed to prevent the recurrence of residual tumors, but these methods lead to toxic side effects and do not provide a long-lasting protection unless frequently repeated.[31] Sustained topical delivery of therapeutic drug cargos with precisely controlled doses for a prolonged time, after surgical resection, may reduce the risk of tumor relapse with minimal side effects and improved convenience of patients and healthcare providers.

The utility of the p-Si needles in the inhibition of postsurgical residual melanoma was tested using C57BL/6 mice and syngeneic B16F10 melanoma cells. The mice were subcutaneously inoculated with 1 × 10^6 B16F10 melanoma cells to mimic a situation where melanoma resection is incomplete and residual cells are present. Following 2 h of the subcutaneous inoculation, an array of the p-Si needles (1 × 1 cm^2, d = 150 nm, D = 1 μm, and L = 50 μm) covalently linked (amide) with 50 μL of DOX (~20 μg) or without DOX (control) was applied to the tumor inoculation site (Figure 5A). The basic procedure for the injection of the p-Si needles (hereinafter referred to as "nanoinjection") is demonstrated in Movie S3 (Supporting Information). A representative photograph in Figure 5B highlights the nanoinjection site on the shaved skin of a mouse. The mouse receiving the p-Si needles moved freely without any sign of discomfort (Movie S4, Supporting Information). Two other control groups of mice were intratumorally administered using a medical 28G insulin syringe (Fisher Scientific, USA) with a single dose of PBS (50 μL) and DOX (50 μL), representing no-treatment control and a conventional bolus injection, respectively. Figure 5C shows that, in the mice treated with the nanoinjection of DOX, tumor growth was suppressed over 10 days postinoculation. In contrast, significant growth of the tumors occurred in 4 out of 5 mice treated with the control nanoinjection (without DOX), all 5 mice with the syringe injection of PBS, and 4 out of 5 mice with the syringe injection of DOX during the same period, followed by rapid increase to reach the end point tumor size of 2000 mm^3 (Figure S15).[32] Figure 5D shows the comparisons of the size of the tumors at 10 days postinoculation. All of these treatments were well tolerated by the mice with negligible weight loss during the survival period (Figure 5E); however, local skin lesions were observed on the mice treated with the syringe injection of DOX (Figure 5F and Figure S16), which is a typical side effect of the drug.[33] The superior antitumor efficacy of the nanoinjected DOX compared to the bolus-injected DOX with the same dose is attributable to the prolonged maintenance of effective local concentration based on the sustained drug release (Figure 3F–H). These findings support that the sustained release of DOX at the skin with residual melanoma cells by nanoinjection can provide a prolonged suppression of tumor growth without adverse effects as compared to a bolus injection. This tendency was also observed in previous reports using polymeric microneedles.[27,34]

https://dx.doi.org/10.1021/acsnano.0c02343
ACS Nano XXXX, XXX, XXX–XXX

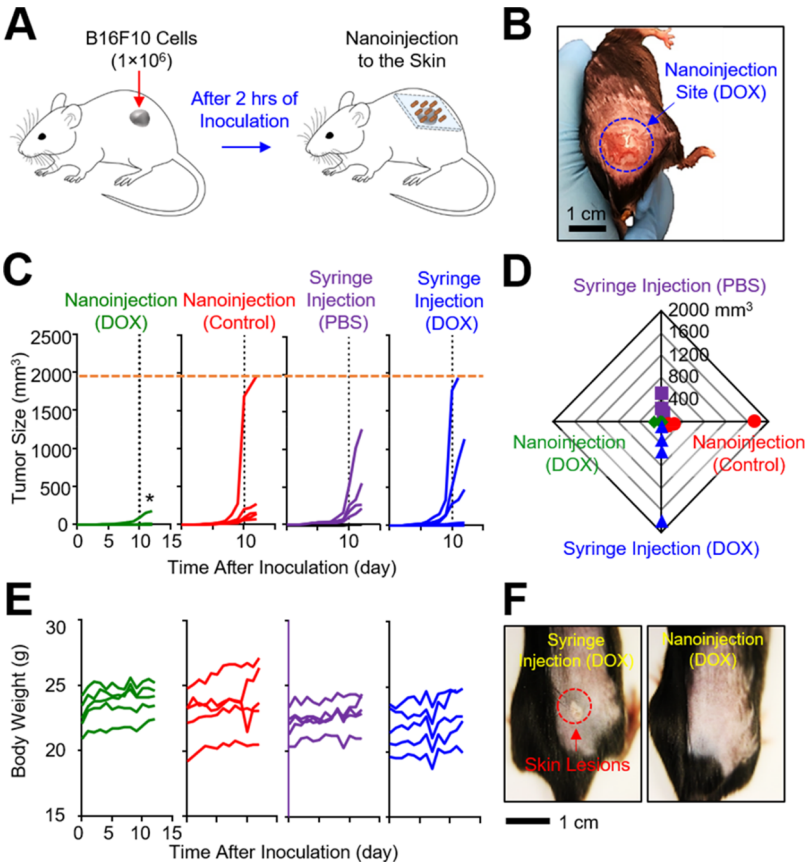

Figure 5. Evaluations in a murine melanoma model *in vivo*. (A) Schematic illustration of experimental protocols for *in vivo* studies in a murine melanoma model. (B) Representative image of the shaved skin of a mouse postnanoinjection of DOX. (C) Measurement results of the tumor size for 12 days postinoculation (n = 5 per group). *p < 0.05 compared to the control syringe injection (DOX) using ANOVA. (D) Radial shape graph of the tumor size at day 10 (n = 5 per group). (E) Measurement results of the body weight for 12 days postinoculation (n = 5 per group). (F) Representative images highlighting the treated sites for 10 days postinjection. The red dotted circle denotes skin lesions.

CONCLUSION

Controlled cracking at the bottom undercut of vertically ordered p-Si needles enables their physical liberation from the rigid Si wafer and subsequent integration with a thin water-soluble backing film over centimeter-scale areas. The water-soluble film serves as a temporary flexible holder that can be seamlessly interfaced with the soft, irregular surface of living tissues during the insertion of the p-Si needles and then immediately dissolved with saline solution. The nanoscale sharpened angular tip of the p-Si needles facilitates their penetration into the epidermis, subcutaneous muscle, and cornea of mice *in vivo* in a minimally invasive manner. The gradual degradation of the p-Si needles in tissue fluids enables the sustained, long-lasting release of preloaded drug cargos. *In vivo* evaluations in a murine melanoma model support the potential utility of this concept in preventing the recurrence of residual melanoma postsurgery. The reported set of materials, structural designs, and assembly method establishes a technical foundation, which can be adjusted and tailored for minimally invasive and painless injection of drug cargos through the cornea for the management of ocular melanomas.[35]

MATERIALS AND METHODS

Fabrication of the p-Si Needles on a Si Wafer. The fabrication began with a bulk Si wafer (p-type; 525 μm thick; 0−100 Ω·cm) by immersing it in a solution of buffered oxide etch (J. T. Baker Inc., USA) for 1 min to eliminate the native oxide layer. Following a standard photolithographic patterning, a deep reactive-ion etching (DRIE) was carried out under a radiofrequency (RF) plasma power of 450 W and a platen power of 11 W using sulfur hexafluoride (SF_6) gas with the flow rate of 85 sccm to create vertically ordered Si micropillars at a prescribed aspect ratio. The deposition of $(C_xF_y)_n$ polymer was followed to form a partial passivation layer using octafluorocyclobutane (C_4F_8) gas with the flow rate of 130 sccm under the RF plasma power of 800 W. Additional isotropic dry etching under the plasma power of 450 W and platen power of 30 W by SF_6 gas with the flow rate of 85 sccm was conducted to create undercuts at the bottom of the Si micropillars. The entire specimen was treated with an oxygen (O_2) plasma (20 sccm, 150 W, 50 mTorr, 15 min), followed by cleaning with standard piranha solution (75% of sulfuric acid (H_2SO_4) and 25% of hydrogen peroxides (H_2O_2)) to eliminate the remaining passivation layer on the surface of the Si micropillars. Finally, the entire specimen was immersed in a solution of potassium hydroxide (KOH; 15 wt %; Fisher Scientific, USA) at 25 °C to reduce the overall size of the Si micropillars down to the nanoscale. The overall size of the miniaturized Si needles was determined by controlling the molarity of etching solution, temperature, and etching time.[15] The next step involved the MACE by immersing the specimen in a mixed solution of 20 mM silver nitrate ($AgNO_3$; Sigma-Aldrich, USA) and 49% hydrofluoric acid (HF; J. T. Baker Inc., USA) to form nanopores on the surface.[36] During the MACE, the overall surface porosity was determined by controlling the etching time. The specimen was then immersed in a solution of Ag etchant (TFS, KI-I2 complex liquid, Transene Inc., USA) for 1 min to remove the remaining Ag residues on the surface. The surface porosity of the resulting p-Si needles was observed using a high-resolution SEM (S-4800, Hitachi, Japan), followed by analyzing the

https://dx.doi.org/10.1021/acsnano.0c02343
ACS Nano XXXX, XXX, XXX−XXX

surface contrast using a post-image processing program (Stream Desktop 2.1, Olympus, Japan) in order to quantify the surface porosity.

Integration of the p-Si Needles with a Water-Soluble Film. The process began by spin-coating a solution of 10 wt % PVA (Mowiol 4-88; Sigma-Aldrich, USA) or 5.5 wt % PLGA (lactide:glycolide (50:50); Sigma-Aldrich, USA) on the as-fabricated p-Si needles on a Si wafer, followed by curing at 70 °C for 30 min. At this stage, the thickness of the water-soluble (PVA or PLGA) film was determined by adjusting the spin-casting speed (in rpm). The spin-coating was repeated until the total thickness of the water-soluble film reached about 200 μm for enhancing the mechanical strength. Finally, the film was mechanically peeled using an automated peeling apparatus (Mark-10, Willrich Precision Instrument) at a constant rate of 50 mm/min, causing cracking at the bottom undercut of the p-Si needles.

Calculation of Theoretical Strain Energy Release Rate (*G*). By measuring the peeling force at low velocity near zero, the theoretical energy release rate was calculated according to the peeling rate. In steady-state crack propagation, the strain energy release rate (G) has the following relation:[37]

$$G = \frac{F}{w} \tag{1}$$

where F is the measured peel force and w is the width of the PVA film. By calculating the critical energy release rate (G_0) at the reference velocity (v_0) near zero, the theoretical energy release rate can be determined as a power law equation:[38]

$$G = G_0\left[1 + \left(\frac{v}{v_0}\right)^n\right] \tag{2}$$

where n is an experimentally measured constant. In the peeling tests, the range of the peeling rate of 2.4−200 mm/min, critical energy release rate (G_0) of 26.15 J/m^2, reference velocity (v_0) of 2.4 mm/min, and experimental constant (n) of 0.14 were determined.

Finite Element Analysis. The FEA was conducted using the ABAQUS/standard package to reveal the underlying mechanics of the p-Si needles under the peeling process. The deformation of the p-Si needles and PVA film was modeled by linear elastic behavior with an E of 112.4 and 3.4 GPa, respectively.[39] The materials were modeled by 8-node solid elements (C_3D_8R). The displacement at constant peeling rate was applied on the top of the PVA film, while a tie constraint was defined at the interface between the p-Si needles and PVA film.

Loading of DOX on the Surface of the p-Si Needles. The process began by washing the as-fabricated p-Si needles on a Si wafer with distilled (DI) water, followed by thorough drying with nitrogen (N_2) gas. The cleaned p-Si needles were immersed in a solution of TESPSA (Gelest Inc., USA) for 2 h to functionalize the surface with amide.[40] Alternatively, the p-Si needles were immersed in a solution of ICPTS (Sigma-Aldrich, USA) for 2 h to functionalize the surface with urea.[41] The p-Si needles were then rinsed with ethanol and then baked at 120 °C for 1 h, followed by immersing in a solution of DOX (0.5 mg/mL; Sigma-Aldrich, USA) for 24 h at room temperature. To prepare the control specimens with physically trapped DOX, the as-fabricated p-Si needles were immersed in a solution of DOX without undergoing any treatment on the surface. The prepared specimens were dried by N_2 gas and stored under an inert atmosphere.

Measurements of Cumulative DOX Release. The p-Si needles loaded with DOX were immersed in a 12-well plate with 4 mL of PBS (pH 7.4 or pH 10.0; Sigma-Aldrich, USA) at 37.5 °C. At the predetermined time intervals, the specimens were sampled and the PBS solution was refreshed. A 100 μL amount of the sampled solution was transferred to a 96-well plate, and the fluorescent intensity was measured with a plate reader (Synergy Neo plate reader, BioTek Instruments). The concentration of the released DOX was determined according to the fluorescent intensity measured with the excitation and emission at 480 and 600 nm, respectively.[42]

Molecular Dynamics Simulations. The MD simulations were conducted to model atomic-scale chemical interactions of Si with H_2O and the associated dissolution dynamics with the Reaxff potential[43] using a large-scale atomic/molecular massively parallel simulator (LAMMPS) package. In these simulations, Si, O, and H were used for the atomic elements.[44] The initial systems included a Si layer with a thickness of 1.2 nm, which was solvated by a box of H_2O with 3090 water molecules. Periodic boundary conditions were used in all directions. The temperature of the system was maintained at 300 K using the Nose-Hoover thermostat, and the time step was selected to be 0.1 fs, in order to ensure the capture of chemical reaction events between the Si and H_2O species.

Cell Viability Tests. For the MTT assay, approximately 5×10^4 HDF cells were seeded on a specimen in a 24-well plate and then incubated for 24, 48, and 72 h. At each measurement point, 200 μL of MTT solution (Sigma-Aldrich, USA) was added to the wells and incubated for 4 h. The cell medium was removed, and 400 μL of dimethyl sulfoxide (C_2H_6OH; Sigma-Aldrich, USA) was added to dissolve precipitated formazan. A 100 μL amount of the solution was transferred to a 96-well plate and measured using a microplate reader (SpectraMax Plus 384 reader, Molecular Devices, USA) at 570 nm.

Acute Inflammation Tests *In Vivo*. All of these animal studies were approved by the Purdue Animal Care and Use Committee (PACUC; #1612001512) for the care and use of laboratory animals. Female athymic nude mice (5−6 weeks old; NCr-Fox1nu, Charles River Laboratories, USA) were used in the acute inflammation tests *in vivo*. As a positive control, 40 μL of PMA (100 μM; Sigma-Aldrich, USA) was rubbed on the epidermis and subcutaneous muscle to induce acute inflammation.[34] The p-Si needles on a PVA film were gently applied to target sites with firm compression. The backing film was then completely dissolved by applying a saline-moistened cotton swab. Following 5 h of the implementation, 100 μL of luminol sodium salt (200 mg/kg; Sigma-Aldrich, USA) was administered by intraperitoneal nanoinjection. Then, the mice were anesthetized with compressed air containing 2.5% isoflurane with a Classic T3 isoflurane vaporizer (Smith Medical, Dublin, OH, USA). Bioluminescence images were acquired using an IVIS Lumina II imaging system (Caliper Life Sciences, USA) for 3 min of exposure time at the F/stop and binning of 1 and 4, respectively.

IVIS Imaging *In Vivo*. All of these animal studies were approved by the Purdue Animal Care and Use Committee (PACUC; #1612001512). The p-Si needles with covalently linked (amide) DyLight 800 dyes were placed on either the epidermis, subcutaneous muscle, or cornea of mice (5−6 weeks old; NCr-Fox1nu, Charles River Laboratories, USA) with firm compression. For the transmuscular nanoinjection, 250 mg/kg of avertin (Sigma-Aldrich, USA) was administrated by an intraperitoneal injection to anesthetize mice, followed by careful incision of the skin with surgical scissors. The incision site was then sutured using a surgical needle and thread. The mice were anesthetized with inhaled isoflurane anesthesia with a Classic T3 isoflurane vaporizer (Smith Medical) and exposed to 2.5% isoflurane delivered in O_2 (2 L/min) within a 1 L induction chamber. The fluorescence of the injection site was measured using an IVIS Lumina II imaging system (Caliper Life Sciences, USA) at day 0, 1, and 2 with an exposure time of 1 s each using a 150 W quartz halogen lamp and then filtered using indocyanine green (ICG) excitation and emission filters with wavelengths of 710−760 and 810−875 nm, respectively. The data analysis was performed using Living Image software (version 4.4, PerkinElmer Inc.).

Demonstration in a Murine Melanoma Model. All of these animal procedures were approved by the Purdue Animal Care and Use Committee (PACUC; #1503001212). Male C57BL/6 mice (8−10 weeks old; Envigo, USA) were acclimatized for at least 1 week prior to the procedures. The p-Si needles were sterilized by an ultraviolet (UV) illumination (254 nm) for 30 min. A total of 10^6 B16F10 melanoma cells (ATCC; Manassas, VA, USA) were subcutaneously inoculated in the bottom flank of the right hind leg of each mouse. After approximately 2 h, the inoculation site was treated with the nanoinjection of the covalently linked (amide) DOX (~20 μg) and the control nanoinjection (without DOX). For

https://dx.doi.org/10.1021/acsnano.0c02343
ACS Nano XXXX, XXX, XXX−XXX

comparison, two other control groups of mice were intratumorally administered using a medical 28G insulin syringe (Fisher, USA) with a single dose of PBS (50 μL) and DOX (20 μg in 50 μL), respectively. The length (L) and width (W) of each tumor were monitored every day using a digital caliper (Thorlabs digital calipers, Thorlabs Inc., USA), and the volume (V) was calculated according to an ellipsoid formula: $V = (L \times W^2)/2$. The body weight of the mice was monitored every other day.

ASSOCIATED CONTENT

Supporting Information

The Supporting Information is available free of charge at https://pubs.acs.org/doi/10.1021/acsnano.0c02343.

Visual observation (16× speed) of a yellow-colored PVA immersed in a solution of PBS (pH 7.4) at 37.5 °C (MP4)

Real-time demonstration of the automated peeling of the p-Si needles from the donor Si wafer (MP4)

Demonstration (26× speed) of the nanoinjection of DOX to the shaved skin of a mouse after 2 h of subcutaneous inoculation with 1 × 10^6 B16F10 melanoma cells (MP4)

Visual observation (2× speed) of a mouse receiving an array (1 × 1 cm^2) of the p-Si needles with covalently linked (amide) DOX on the back side (MP4)

SEM images, optical images, FEA results, MTT assay results, microscope images, schematic diagrams, measurement results (PDF)

AUTHOR INFORMATION

Corresponding Authors

Yoon Yeo − *Department of Industrial and Physical Pharmacy, Purdue University, West Lafayette, Indiana 47907, United States;* orcid.org/0000-0001-9505-7701; Email: yyeo@purdue.edu

Dong Rip Kim − *School of Mechanical Engineering, Hanyang University, Seoul, South Korea;* orcid.org/0000-0001-6398-9483; Email: dongrip@hanyang.ac.kr

Chi Hwan Lee − *Weldon School of Biomedical Engineering, School of Mechanical Engineering, School of Materials Engineering, and Department of Speech, Language, and Hearing Sciences, Purdue University, West Lafayette, Indiana 47907, United States;* orcid.org/0000-0002-4868-7054; Email: lee2270@purdue.edu

Authors

Hyungjun Kim − *Weldon School of Biomedical Engineering and Department of Industrial and Physical Pharmacy, Purdue University, West Lafayette, Indiana 47907, United States*

Heung Soo Lee − *School of Mechanical Engineering, Hanyang University, Seoul, South Korea;* orcid.org/0000-0002-9393-0121

Yale Jeon − *School of Mechanical Engineering, Hanyang University, Seoul, South Korea*

Woohyun Park − *School of Mechanical Engineering, Purdue University, West Lafayette, Indiana 47907, United States*

Yue Zhang − *Department of Mechanical and Aerospace Engineering, University of Virginia, Charlottesville, Virginia 22904, United States*

Bongjoong Kim − *School of Mechanical Engineering, Purdue University, West Lafayette, Indiana 47907, United States;* orcid.org/0000-0002-9969-6954

Hanmin Jang − *School of Mechanical Engineering, Hanyang University, Seoul, South Korea;* orcid.org/0000-0002-7724-4244

Baoxing Xu − *Department of Mechanical and Aerospace Engineering, University of Virginia, Charlottesville, Virginia 22904, United States;* orcid.org/0000-0002-2591-8737

Complete contact information is available at: https://pubs.acs.org/10.1021/acsnano.0c02343

Author Contributions

#H.K. and H.L. contributed equally to this work.

Notes

The authors declare no competing financial interest.

ACKNOWLEDGMENTS

C.H.L. acknowledges funding support from the Asian Office of Aerospace Research & Development (AOARD: FA2386-16-1-4105; program manager: Dr. Tony Kim) and the Air Force Office of Scientific Research (AFOSR: FA2386-18-1-40171; program manager: Dr. Tony Kim). D.R.K. acknowledges funding support from the International Research and Development Program (NRF-2018K1A3A1A32055469) and the Basic Science Research Program (NRF-2018R1C1B6007938) through the National Research Foundation of Korea (NRF) funded by the Ministry of Science and ICT of Korea. Y.Y. acknowledges funding support from the National Institutes of Health (NIH: R01 CA199663). B.X. acknowledges funding support on chemomechanics of reactive MD simulations from National Science Foundation (NSF-CMMI-1728149).

REFERENCES

(1) Simoes, M. C. F.; Sousa, J. J. S.; Pais, A. Skin Cancer and New Treatment Perspectives: A Review. *Cancer Lett.* **2015**, *357*, 8−42.

(2) Perera, E.; Gnaneswaran, N.; Jennens, R.; Sinclair, R. Malignant Melanoma. *Healthcare* **2014**, *2*, 1−19.

(3) Prausnitz, M. R.; Langer, R. Transdermal Drug Delivery. *Nat. Biotechnol.* **2008**, *26*, 1261−1268.

(4) Li, W.; Terry, R. N.; Tang, J.; Feng, M. H. R.; Schwendeman, S. P.; Prausnitz, M. R. Rapidly Separable Microneedle Patch for the Sustained Release of a Contraceptive. *Nat. Biomed. Eng.* **2019**, *3*, 220−230.

(5) Gopal, S.; Chiappini, C.; Penders, J.; Leonardo, V.; Seong, H.; Rothery, S.; Korchev, Y.; Shevchuk, A.; Stevens, M. M. Porous Silicon Nanoneedles Modulate Endocytosis to Deliver Biological Payloads. *Adv. Mater.* **2019**, *31*, 1−8.

(6) Chiappini, C.; De Rosa, E.; Martinez, J.; Liu, X.; Steele, J.; Stevens, M.; Tasciotti, E. Biodegradable Silicon Nanoneedles Delivering Nucleic Acids Intracellularly Induce Localized *In Vivo* Neovascularization. *Nat. Mater.* **2015**, *14*, 532−539.

(7) Chiappini, C.; Martinez, J.; De Rosa, E.; Almeida, C.; Tasciotti, E.; Stevens, M. Biodegradable Nanoneedles for Localized Delivery of Nanoparticles *In Vivo*: Exploring the Biointerface. *ACS Nano* **2015**, *9*, 5500−5509.

(8) Fang, Y.; Jiang, Y. W.; Ledesrna, H. A.; Yi, J. S.; Gao, X.; Weiss, D. E.; Shi, F. Y.; Tian, B. Z. Texturing Silicon Nanowires for Highly Localized Optical Modulation of Cellular Dynamics. *Nano Lett.* **2018**, *18*, 4487−4492.

(9) Anglin, E. J.; Cheng, L. Y.; Freeman, W. R.; Sailor, M. J. Porous Silicon in Drug Delivery Devices and Materials. *Adv. Drug Delivery Rev.* **2008**, *60*, 1266−1277.

(10) Lee, Y. K.; Yu, K. J.; Song, E. M.; Farimani, A. B.; Vitale, F.; Xie, Z. Q.; Yoon, Y.; Kim, Y.; Richardson, A.; Luan, H. W.; Wu, Y. X.; Xie, X.; Lucas, T. H.; Crawford, K.; Mei, Y. F.; Feng, X.; Huang, Y. G.; Litt, B.; Aluru, N. R.; Yin, L.; et al. Dissolution of Monocrystalline Silicon Nanomembranes and Their Use as Encapsulation Layers and

https://dx.doi.org/10.1021/acsnano.0c02343
ACS Nano XXXX, XXX, XXX−XXX

Electrical Interfaces in Water-Soluble Electronics. *ACS Nano* **2017**, *11*, 12562−12572.
(11) Hwang, S.; Park, G.; Edwards, C.; Corbin, E.; Kang, S.; Cheng, H.; Song, J.; Kim, J.; Yu, S.; Ng, J.; Lee, J.; Kim, J.; Yee, C.; Bhaduri, B.; Su, Y.; Omennetto, F.; Huang, Y.; Bashir, R.; Goddard, L.; Popescu, G.; et al. Dissolution Chemistry and Biocompatibility of Single-Crystalline Silicon Nanomembranes and Associated Materials for Transient Electronics. *ACS Nano* **2014**, *8*, 5843−5851.
(12) Santos, H. A.; Makila, E.; Airaksinen, A. J.; Bimbo, L. M.; Hirvonen, J. Porous Silicon Nanoparticles for Nanomedicine: Preparation and Biomedical Applications. *Nanomedicine* **2014**, *9*, 535−554.
(13) Abbott, J.; Ye, T. Y.; Ham, D.; Park, H. Optimizing Nanoelectrode Arrays for Scalable Intracellular Electrophysiology. *Acc. Chem. Res.* **2018**, *51*, 600−608.
(14) Jovanovic, P.; Mihajlovic, M.; Djordjevic-Jocic, J.; Vlajkovic, S.; Cekic, S.; Stefanovic, V. Ocular Melanoma: An Overview of the Current Status. *Int. J. Clin. Exp. Pathol.* **2013**, *6*, 1230−1244.
(15) Kim, H.; Jang, H.; Kim, B.; Kim, M. K.; Wie, D. S.; Lee, H. S.; Kim, D. R.; Lee, C. H. Flexible Elastomer Patch with Vertical Silicon Nanoneedles for Intracellular and Intratissue Nanoinjection of Biomolecules. *Sci. Adv.* **2018**, *4*, 1−8.
(16) Lim, J.; Tahk, D.; Yu, J.; Min, D. H.; Jeon, N. L. Design Rules for a Tunable Merged-Tip Microneedle. *Microsyst. & Nanoeng.* **2018**, *4*, 1−10.
(17) Meitl, M.; Zhu, Z.; Kumar, V.; Lee, K.; Feng, X.; Huang, Y.; Adesida, I.; Nuzzo, R.; Rogers, J. Transfer Printing by Kinetic Control of Adhesion to an Elastomeric Stamp. *Nat. Mater.* **2006**, *5*, 33−38.
(18) Wang, L.; Gao, Y.; Dai, F. Q.; Kong, D. Y.; Wang, H. C.; Sun, P. C.; Shi, Z.; Sheng, X.; Xu, B. X.; Yin, L. Geometrical and Chemical-Dependent Hydrolysis Mechanisms of Silicon Nanomembranes for Biodegradable Electronics. *ACS Appl. Mater. Interfaces* **2019**, *11*, 18013−18023.
(19) Yin, L.; Farimani, A.; Min, K.; Vishal, N.; Lam, J.; Lee, Y.; Aluru, N.; Rogers, J. Mechanisms for Hydrolysis of Silicon Nanomembranes as Used in Bioresorbable Electronics. *Adv. Mater.* **2015**, *27*, 1−8.
(20) Chang, J. K.; Emon, M. A. B.; Li, C. S.; Yang, Q. S.; Chang, H. P.; Yang, Z. J.; Wu, C. I.; Saif, M. T.; Rogers, J. A. Cytotoxicity and *In Vitro* Degradation Kinetics of Foundry-Compatible Semiconductor Nanomembranes and Electronic Microcomponents. *ACS Nano* **2018**, *12*, 9721−9732.
(21) Muller, A. J.; Sharma, M. D.; Chandler, P. R.; DuHadaway, J. B.; Everhart, M. E.; Johnson, B. A.; Kahler, D. J.; Pihkala, J.; Soler, A. P.; Munn, D. H.; Prendergast, G. C.; Mellor, A. L. Chronic Inflammation that Facilitates Tumor Progression Creates Local Immune Suppression by Inducing Indoleamine 2,3 Dioxygenase. *Proc. Natl. Acad. Sci. U. S. A.* **2008**, *105*, 17073−17078.
(22) Gross, S.; Gammon, S. T.; Moss, B. L.; Rauch, D.; Harding, J.; Heinecke, J. W.; Ratner, L.; Piwnica-Worms, D. Bioluminescence Imaging of Myeloperoxidase Activity *In Vivo*. *Nat. Med.* **2009**, *15*, 455−461.
(23) Pei, P.; Yang, F.; Liu, J. X.; Hu, H. R.; Du, X. Y.; Hanagata, N.; Zhao, S. C.; Zhu, Y. F. Composite-Dissolving Microneedle Patches for Chemotherapy and Photothermal Therapy in Superficial Tumor Treatment. *Biomater. Sci.* **2018**, *6*, 1414−1423.
(24) Ahmed, K. S.; Shan, X.; Mao, J.; Qiu, L.; Chen, J. Derma Roller Microneedles-Mediated Transdermal Delivery of Doxorubicin and Celecoxib Co-Loaded Liposomes for Enhancing the Anticancer Effect. *Mater. Sci. Eng., C* **2019**, *99*, 1448−1458.
(25) Wang, Z. H.; Gangarapu, S.; Escorihuela, J.; Fei, G. X.; Zuilhof, H.; Xia, H. S. Dynamic Covalent Urea Bonds and Their Potential for Development of Self-Healing Polymer Materials. *J. Mater. Chem. A* **2019**, *7*, 15933−15943.
(26) Wu, E. C.; Park, J.-H.; Park, J.; Segal, E.; Cunin, F.; Sailor, M. J. Oxidation-Triggered Release of Fluorescent Molecules or Drugs from Mesoporous Si Microplarticles. *ACS Nano* **2008**, *2*, 2401−2409.
(27) Bhatnagar, S.; Bankar, N. G.; Kulkarni, M. V.; Venuganti, V. V. K. Dissolvable Microneedle Patch Containing Doxorubicin and Docetaxel is Effective in 4T1 Xenografted Breast Cancer Mouse Model. *Int. J. Pharm.* **2019**, *556*, 263−275.
(28) Chen, M. C.; Lin, Z. W.; Ling, M. H. Near-Infrared Light-Activatable Microneedle System for Treating Superficial Tumors by Combination of Chemotherapy and Photothermal Therapy. *ACS Nano* **2016**, *10*, 93−101.
(29) Sullivan, S. P.; Koutsonanos, D. G.; Martin, M. D.; Lee, J. W.; Zarnitsyn, V.; Choi, S. O.; Murthy, N.; Compans, R. W.; Skountzou, I.; Prausnitz, M. R. Dissolving Polymer Microneedle Patches for Influenza Vaccination. *Nat. Med.* **2010**, *16*, 1−7.
(30) Chen, Q.; Wang, C.; Zhang, X.; Chen, G.; Hu, Q.; Li, H.; Wang, J.; Wen, D.; Zhang, Y.; Lu, Y.; Yang, G.; Jiang, C.; Wang, J.; Dotti, G.; Gu, Z. *In Situ* Sprayed Bioresponsive Immunotherapeutic Gel for Post-Surgical Cancer Treatment. *Nat. Nanotechnol.* **2019**, *14*, 89−98.
(31) Albain, K. S.; Swann, R. S.; Rusch, V. W.; Turrisi, A. T., III; Shepherd, F. A.; Smith, C.; Chen, Y.; Livingston, R. B.; Feins, R. H.; Gandara, D. R.; Fry, W. A.; Darling, G.; Johnson, D. H.; Green, M. R.; Miller, R. C.; Ley, J.; Sause, W. T.; Cox, J. D. Radiotherapy Plus Chemotherapy with or without Surgical Resection for Stage III Non-Small-Cell Lung Cancer: A Phase III Randomised Controlled Trial. *Lancet* **2009**, *374*, 379−386.
(32) Xu, J.; Lee, S. S.-Y.; Seo, H.; Pang, L.; Jun, Y.; Zhang, R.-Y.; Zhang, Z.-Y.; Kim, P.; Lee, W.; Kron, S. J.; Yeo, Y. Quinic Acid-Conjugated Nanoparticles Enhance Drug Delivery to Solid Tumors *via* Interactions with Endothelial Selectins. *Small* **2018**, *14*, 1−16.
(33) Lotem, M.; Hubert, A.; Lyass, O.; Goldenhersh, M. A.; Lngber, A.; Peretz, T.; Gabizon, A. Skin Toxic Effects of Polyethylene Glycol-Coated Liposomal Doxorubicin. *Arch. Dermatol.* **2000**, *136*, 1475−1480.
(34) Kubicka-Wolkowska, J.; Kedzierska, M.; Lisik-Habib, M.; Potemski, P. Skin Toxicity in a Patient with Ovarian Cancer Treated with Pegylated Liposomal Doxorubicin: A Case Report and Review of the Literature. *Oncol. Lett.* **2016**, *12*, 5332−5334.
(35) Sassalos, T. M.; Paulus, Y. M. Prefilled Syringes for Intravitreal Drug Delivery. *Clin. Ophthalmol.* **2019**, *13*, 701−706.
(36) Han, H.; Huang, Z.; Lee, W. Metal-Assisted Chemical Etching of Silicon and Nanotechnology Applications. *Nano Today* **2014**, *9*, 271−304.
(37) Feng, X.; Meitl, M. A.; Bowen, A. M.; Huang, Y.; Nuzzo, R. G.; Rogers, J. A. Competing Fracture in Kinetically Controlled Transfer Printing. *Langmuir* **2007**, *23*, 12555−12560.
(38) Chen, H.; Feng, X.; Huang, Y.; Huang, Y. G.; Rogers, J. A. Experiments and Viscoelastic Analysis of Peel Test with Patterned Strips for Applications to Transfer Printing. *J. Mech. Phys. Solids* **2013**, *61*, 1737−1752.
(39) Ryu, S.; Xiao, J.; Park, W.; Son, K.; Huang, Y.; Paik, U.; Rogers, J. Lateral Buckling Mechanics in Silicon Nanowires on Elastomeric Substrates. *Nano Lett.* **2009**, *9*, 3214−3219.
(40) Gang, A.; Gabernet, G.; Renner, L. D.; Baraban, L.; Cuniberti, G. A Simple Two-Step Silane-Based (Bio-) Receptor Molecule Immobilization without Additional Binding Site Passivation. *RSC Adv.* **2015**, *5*, 35631−35634.
(41) Escorihuela, J.; Jose Banuls, M.; Garcia Castello, J.; Toccafondo, V.; Garcia-Ruperez, J.; Puchades, R.; Maquieira, A. Chemical Silicon Surface Modification and Bioreceptor Attachment to Develop Competitive Integrated Photonic Biosensors. *Anal. Bioanal. Chem.* **2012**, *404*, 2831−2840.
(42) Shah, S.; Chandra, A.; Kaur, A.; Sabnis, N.; Lacko, A.; Gryczynski, Z.; Fudala, R.; Gryczynski, I. Fluorescence Properties of Doxorubicin in PBS Buffer and PVA Films. *J. Photochem. Photobiol., B* **2017**, *170*, 65−69.
(43) Zhang, Y.; Kim, B. O. O.; Gao, Y.; Wie, D. S.; Lee, C. H.; Xu, B. X. Chemomechanics of Transfer Printing of Thin Films in a Liquid Environment. *Int. J. Solids Struct.* **2019**, *180*, 30−44.
(44) Fogarty, J. C.; Aktulga, H. M.; Grama, A. Y.; van Duin, A. C. T.; Pandit, S. A. A Reactive Molecular Dynamics Simulation of the Silica-Water Interface. *J. Chem. Phys.* **2010**, *132*, 1−10.

https://dx.doi.org/10.1021/acsnano.0c02343
ACS Nano XXXX, XXX, XXX−XXX

Supporting Information

Bioresorbable, Miniaturized Porous Silicon Needles on a Flexible Water-Soluble Backing for Unobtrusive, Sustained Delivery of Chemotherapy

Hyungjun Kim[†,‡,#], Heung Soo Lee[§,#], Yale Jeon[§], Woohyun Park[¥], Yue Zhang[‖], Bongjoong Kim[¥], Hanmin Jang[§], Baoxing Xu[‖], Yoon Yeo[‡], Dong Rip Kim[§]*, Chi Hwan Lee[†,¥,⊥,£]**

[†]Weldon School of Biomedical Engineering, Purdue University, West Lafayette, Indiana 47907, United States
[‡]Department of Industrial and Physical Pharmacy, Purdue University, West Lafayette, Indiana 47907, United States
[§]School of Mechanical Engineering, Hanyang University, Seoul, South Korea
[¥]School of Mechanical Engineering, Purdue University, West Lafayette, Indiana 47907, United States
[‖] Department of Mechanical and Aerospace Engineering, University of Virginia, Charlottesville, Virginia 22904, United States
[⊥]School of Materials Engineering, Purdue University, West Lafayette, Indiana 47907, United States [£]Department of Speech, Language, and Hearing Sciences, Purdue University, West Lafayette, Indiana 47907, United States

KEYWORDS: *melanoma treatment, topical drug delivery, bioresorbable silicon nanomaterials, sustained drug release, minimally invasive injection*

Supplementary Movie Legends

Movie S1. Visual observation (16× speed) of a yellow-colored PVA immersed in a solution of PBS (pH 7.4) at 37.5 °C.

Movie S2. Real-time demonstration of the automated peeling of the p-Si needles from the donor Si wafer

Movie S3. Demonstration (26× speed) of the nanoinjection of DOX to the shaved skin of a mouse after 2 h of subcutaneous inoculation with 1×10^6 B16F10 melanoma cells.

Movie S4. Visual observation (2× speed) of a mouse receiving an array (1×1 cm^2) of the p-Si needles with covalently-linked (amide) DOX on the back side.

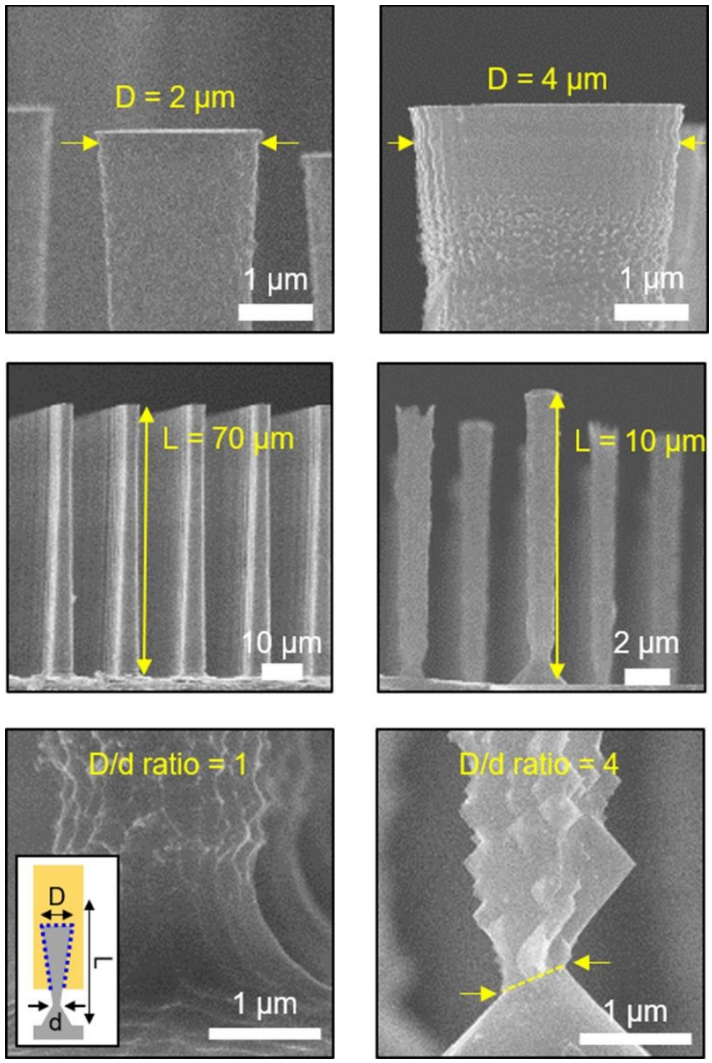

Figure S1. SEM images of the p-Si needles fabricated on a donor Si wafer with varied geometries. The inset schematic image denotes the base diameter (D) and undercut diameter (d) of the p-Si needles.

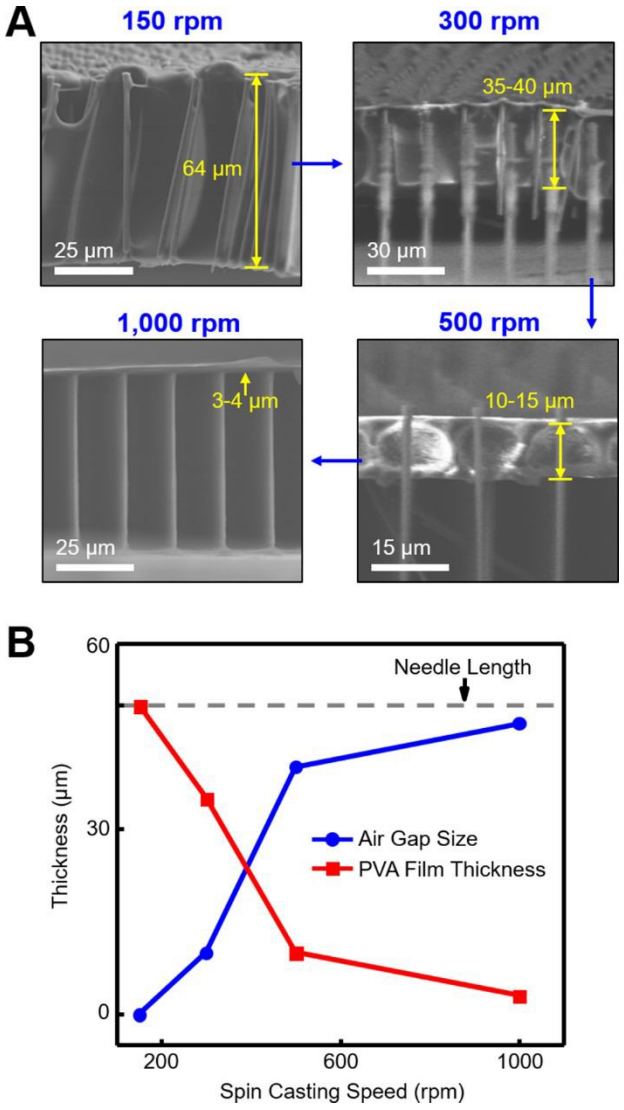

Figure S2. (A) SEM images of the PVA film coated on the p-Si needles at varied spin-casting speeds of 150, 300, 500, and 1,000 rpm from the left. (B) Plot of the measured thicknesses of the PVA film and air gap size as a function of spin casting speed ranging from 150 rpm to 1,000 rpm.

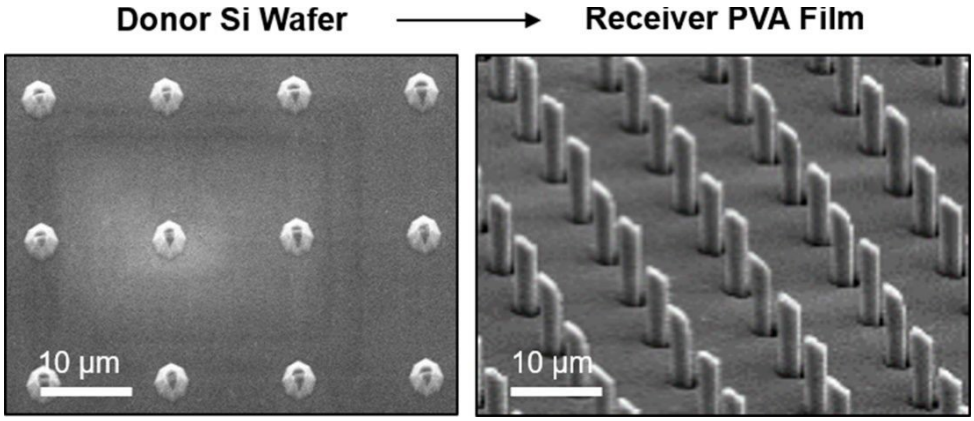

Figure S3. SEM images of a donor Si wafer (left image) and receiver PVA film (right image).

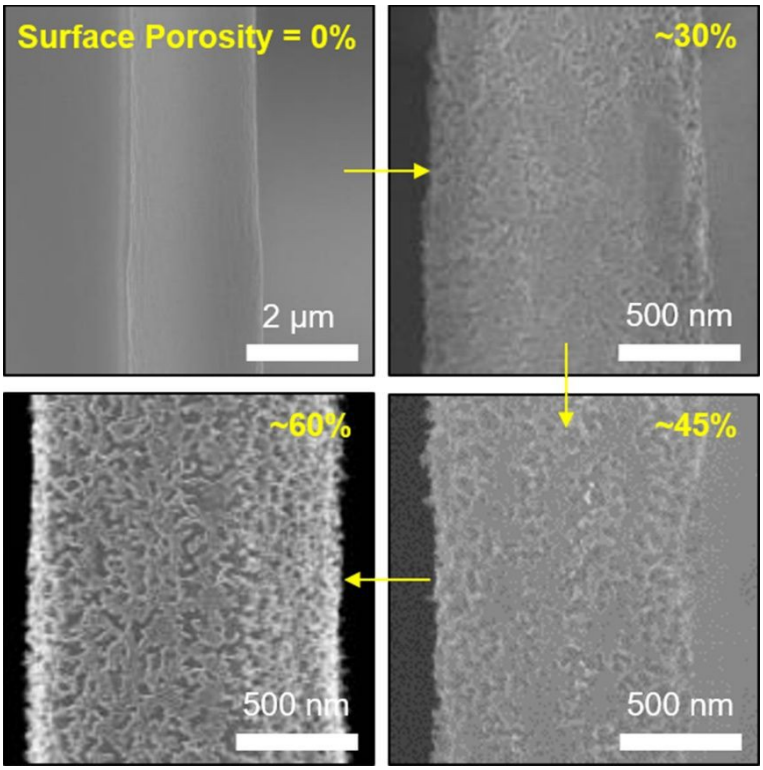

Figure S4. SEM images of the p-Si needles with varied surface porosities of 0%, 30%, 45%, and 60%.

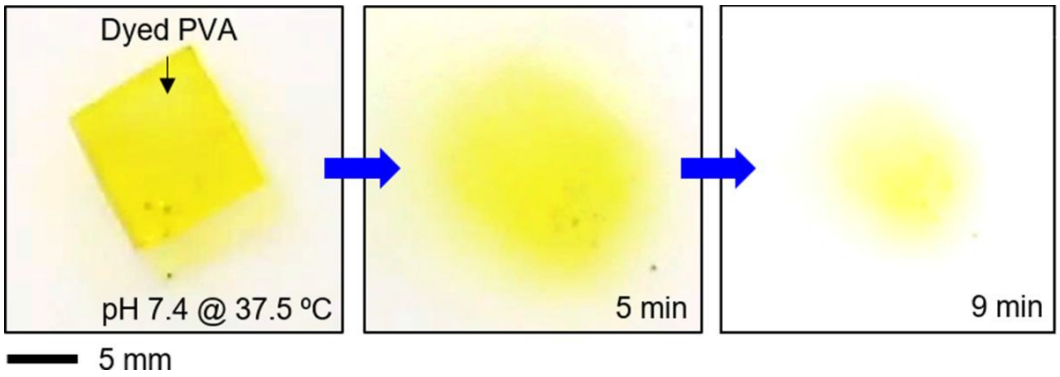

Figure S5. Time-dependent optical images of a yellow-colored PVA film immersed in a solution of PBS (pH 7.4) at 37.5 °C.

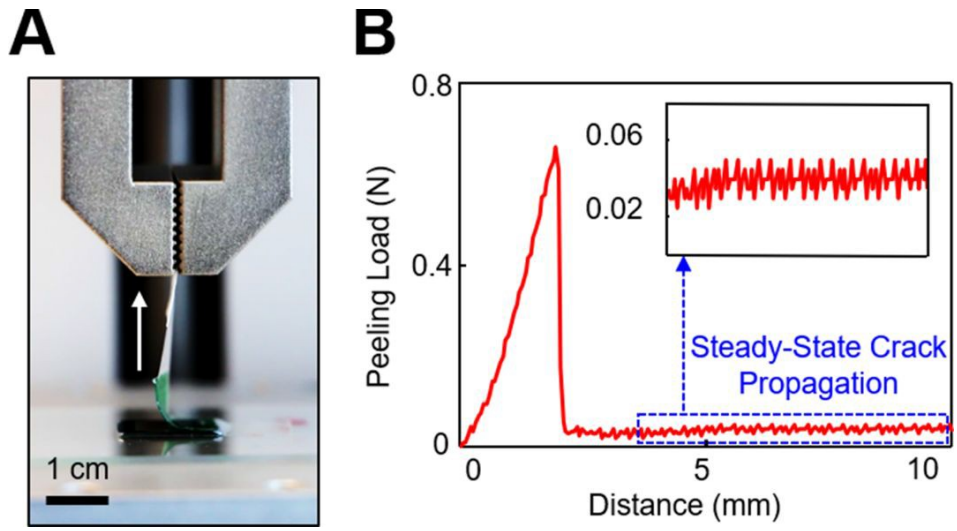

Figure S6. (A) Optical image of an experimental setup for the automated peeling of the p-Si needles from the donor Si wafer. (B) Measurement results of the peeling load obtained from a unit specimen (1×1 cm^2).

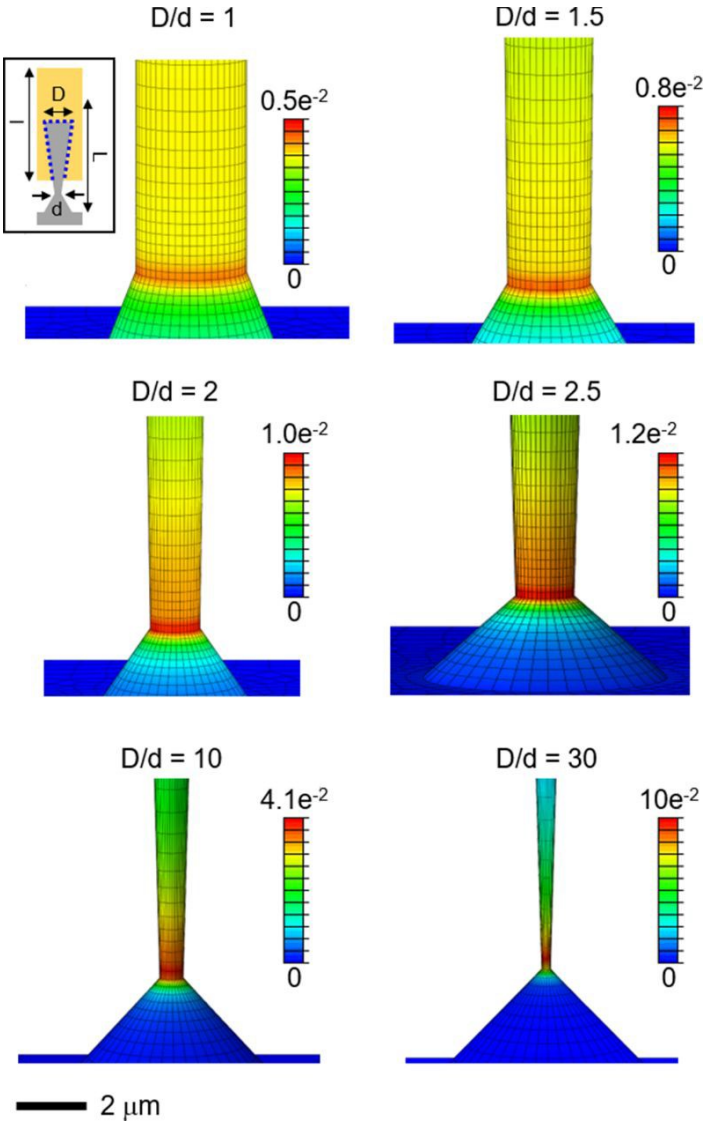

Figure S7. FEA results displaying the distribution of principal strains along the p-Si nanoneedle with varied D/d ratios under constant mechanical peeling.

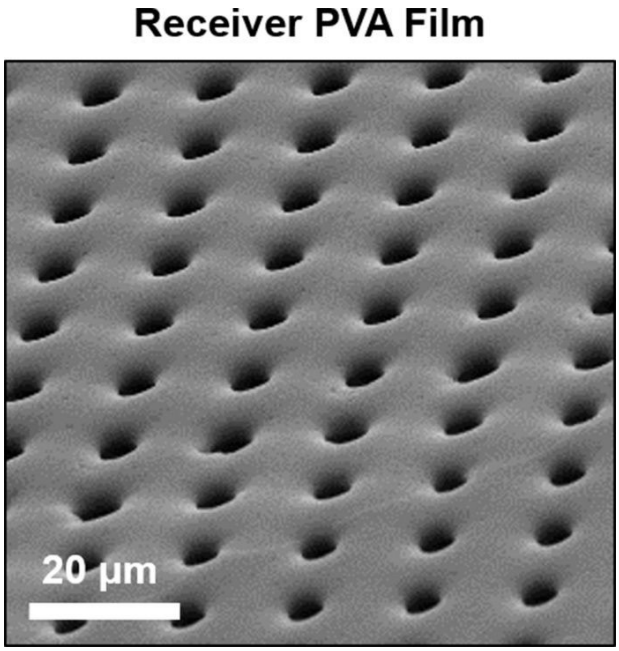

Figure S8. Representative SEM image displaying the compressed marks leftover on the surface of a PVA film peeled out of optimal conditions.

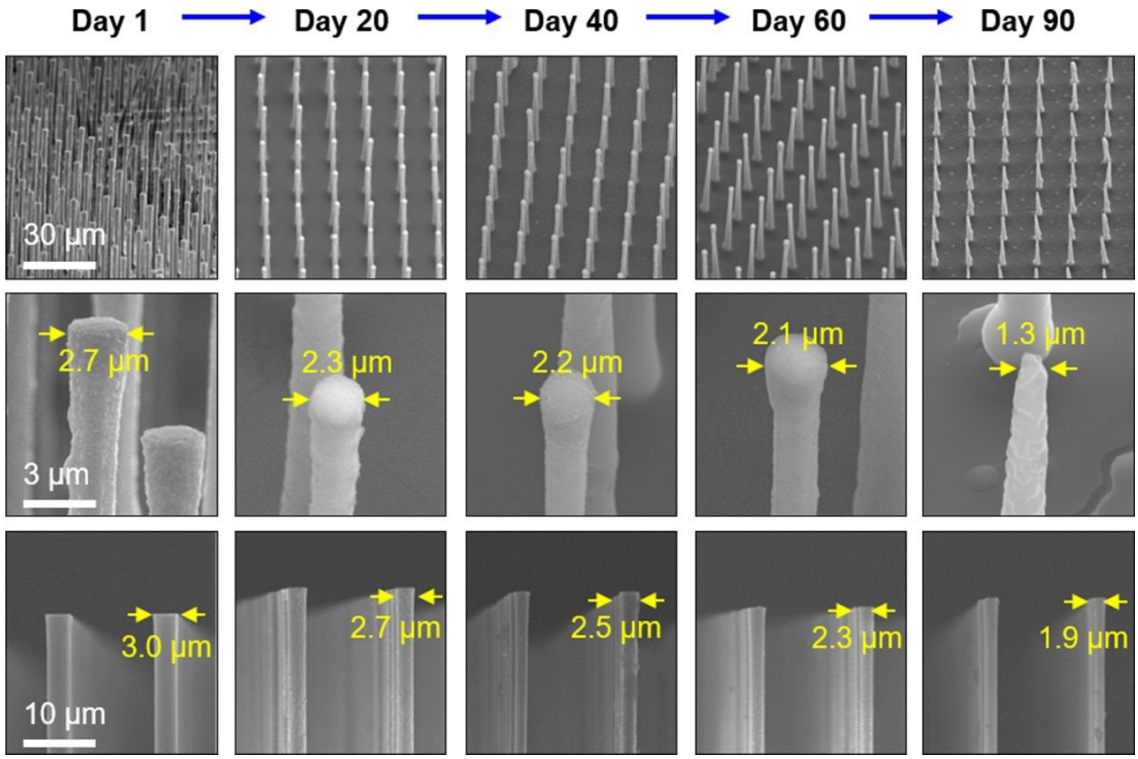

Figure S9. SEM images of the p-Si needles immersed in 50 ml of PBS (pH 7.4) at 37.5 °C for 90 days.

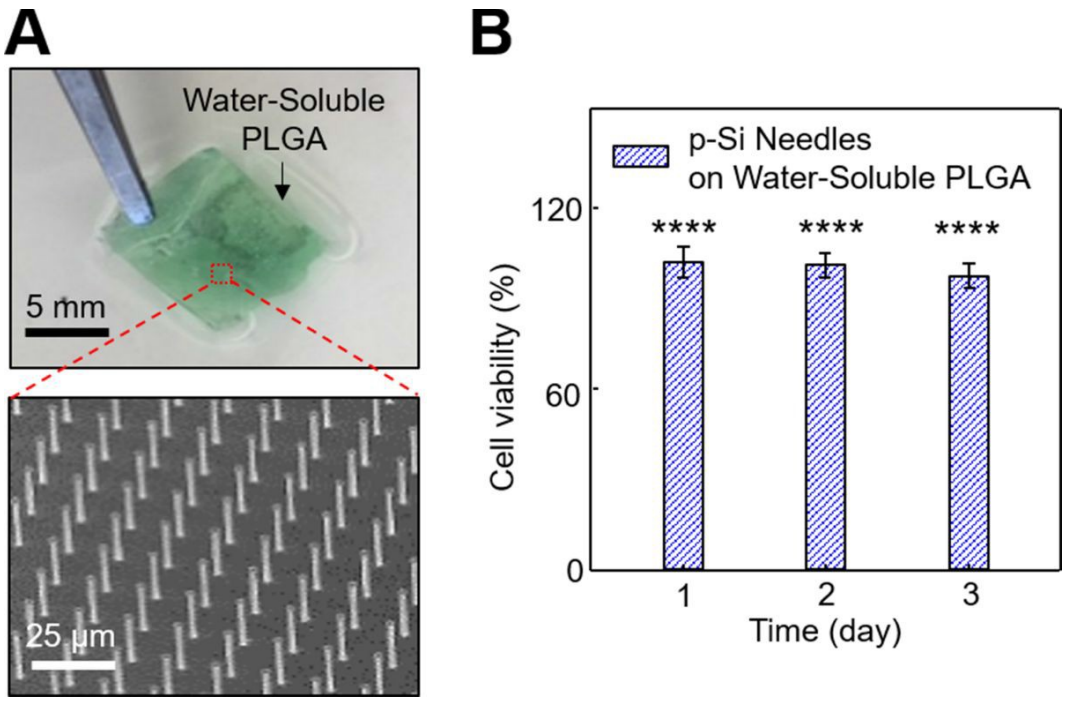

Figure S10. (A) Photograph (top panel) and SEM (bottom panel) images of the p-Si needles built on a water-soluble PLGA film. (B) Corresponding results of MTT assay for the cytotoxicity test of HDF cells. Error bars represent the SD of the three replicates. ****$p<0.0001$ compared to the industrial-grade PVA with the p-Si needles using ANOVA.

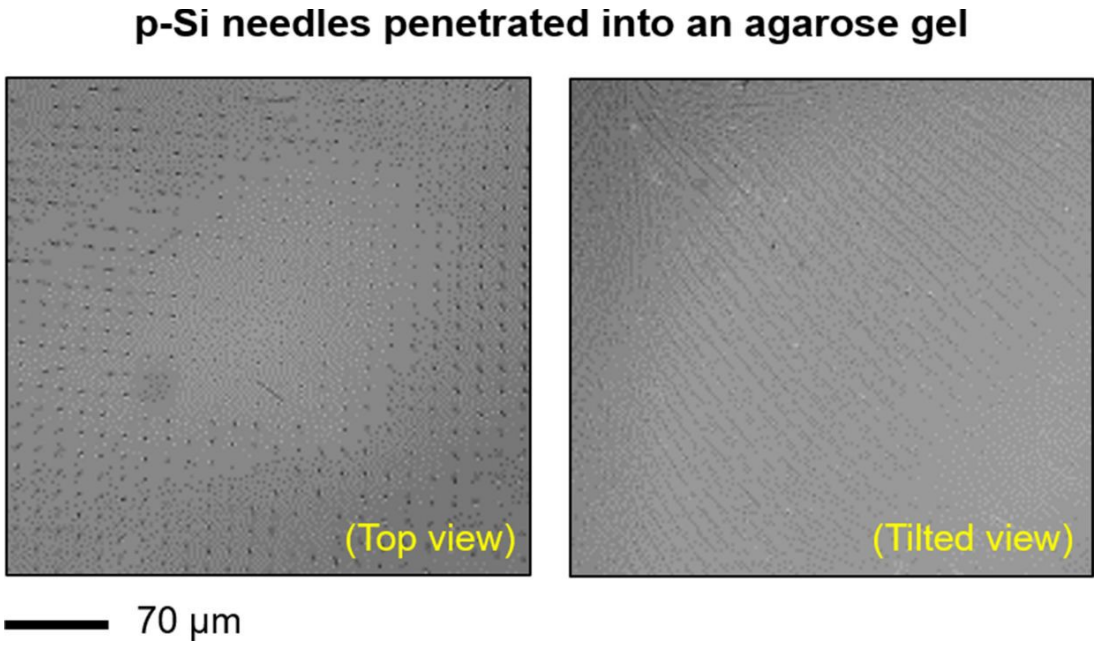

Figure S11. Top-view (left image) and tilted-view (right image) microscope images of the p-Si needles penetrated into a 2.8% (w/v) agarose gel.

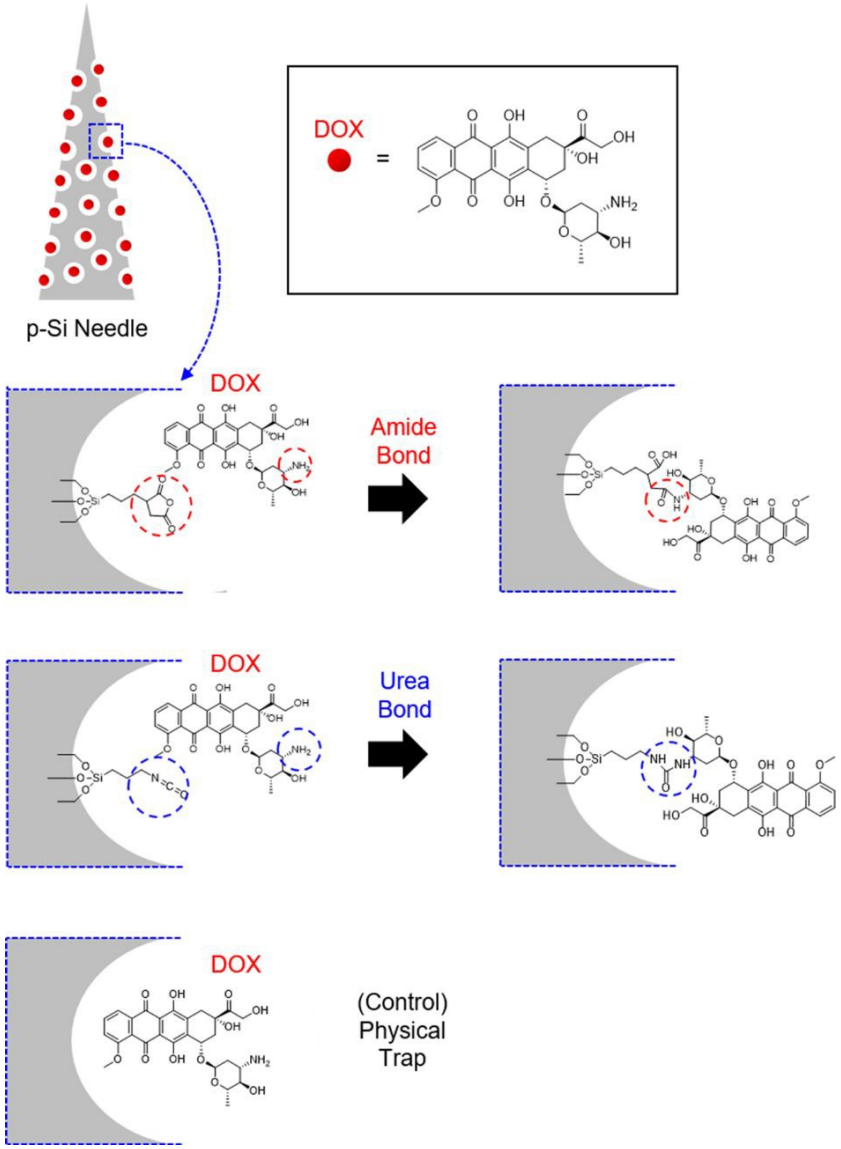

Figure S12. Schematic diagrams of the amide, urea, and physical bonds of DOX to the surface of the p-Si needles.

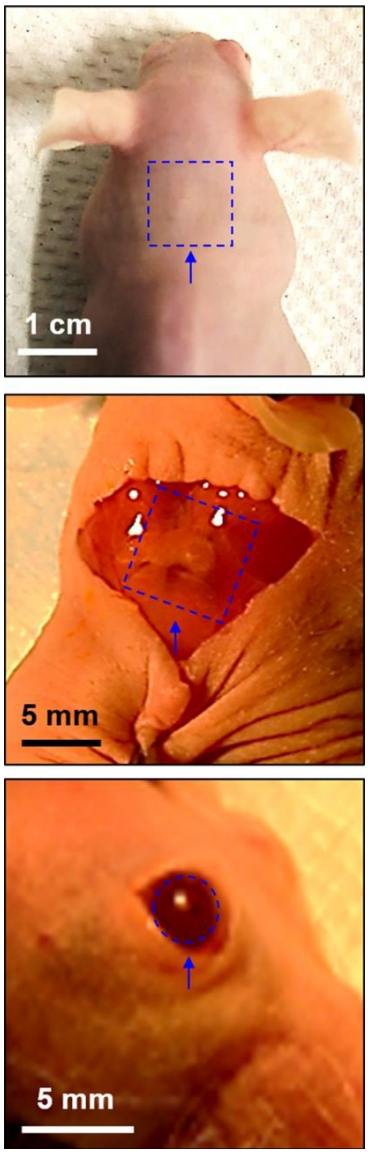

Figure S13. Enlarged optical images of the epidermis, subcutaneous muscle, and cornea of mice receiving the p-Si needles

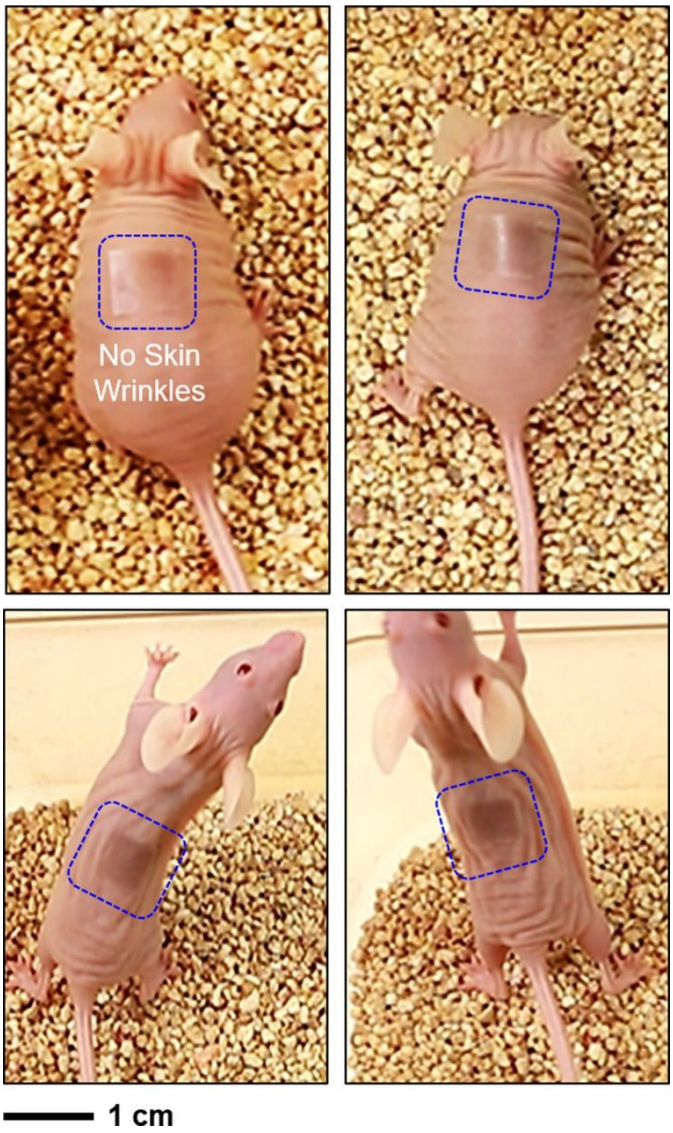

Figure S14. Optical images of a nude mouse worn with the control p-Si needles built on a PDMS film on the backsdie.

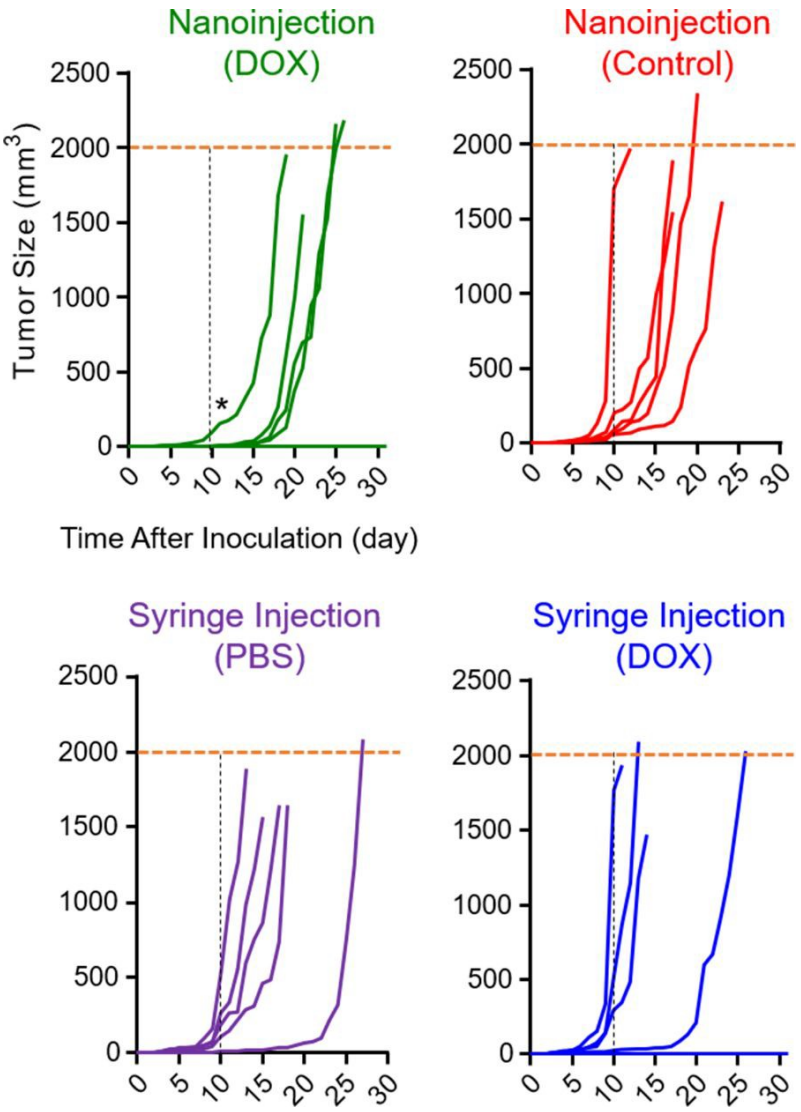

Figure S15. Measurement results of the tumor size (n = 5 per group). The mice were humanely sacrificed when the tumor size reached the endpoint of 2,000 mm^3. *$p<0.05$, compared to the control syringe injection (DOX) using ANOVA.

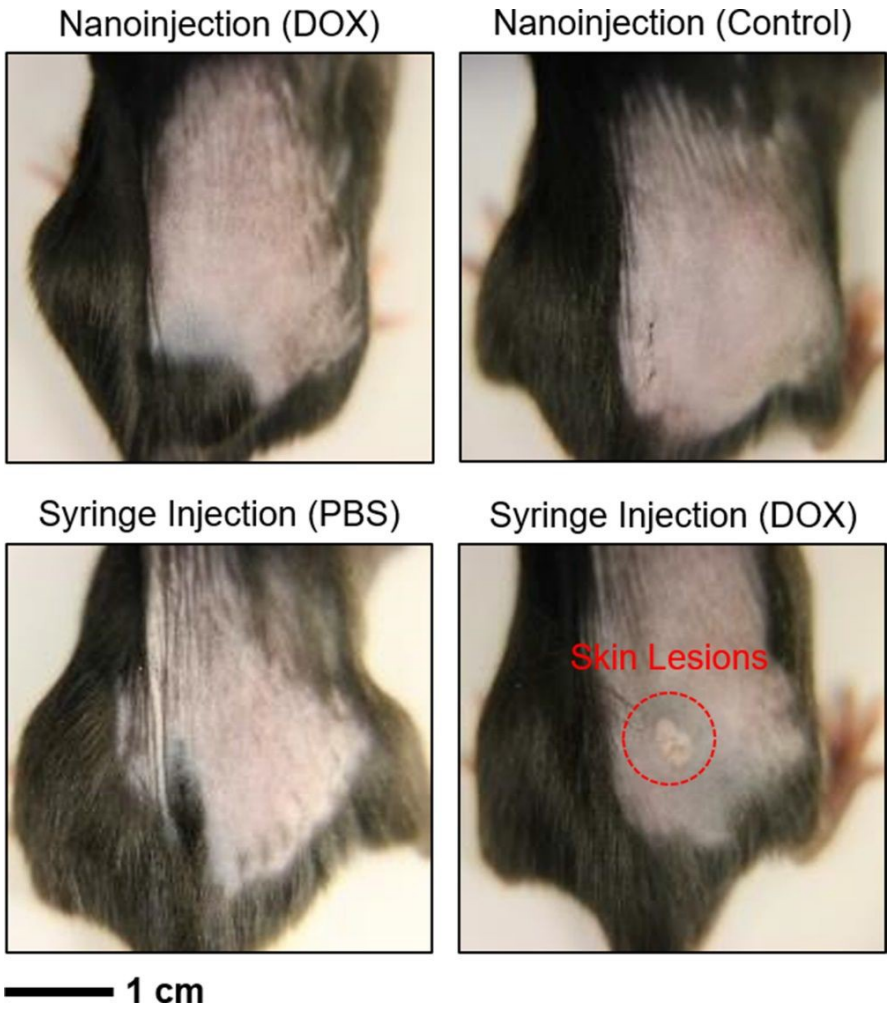

Figure S16. Enlarged optical images of the treated sites of the mice at 10 days post-injection